

COMPUTATIONAL MODELING OF RUPTURE IN RUBBERY POLYMERS

A THESIS SUBMITTED TO  
THE GRADUATE SCHOOL OF NATURAL AND APPLIED SCIENCES  
OF  
MIDDLE EAST TECHNICAL UNIVERSITY

BY

BERKAY AKÇÖREN

IN PARTIAL FULFILLMENT OF THE REQUIREMENTS  
FOR  
THE DEGREE OF MASTER OF SCIENCE  
IN  
CIVIL ENGINEERING

JANUARY 2020



Approval of the thesis:

**COMPUTATIONAL MODELING OF RUPTURE IN RUBBERY POLYMERS**

submitted by **BERKAY AKÇÖREN** in partial fulfillment of the requirements for the degree of **Master of Science in Civil Engineering Department, Middle East Technical University** by,

Prof. Dr. Halil Kalıpçılar  
Dean, Graduate School of **Natural and Applied Sciences**

\_\_\_\_\_

Prof. Dr. Ahmet Türer  
Head of Department, **Civil Engineering**

\_\_\_\_\_

Assoc. Prof. Dr. Serdar Göktepe  
Supervisor, **Civil Engineering, METU**

\_\_\_\_\_

**Examining Committee Members:**

Prof. Dr. Kağan Tuncay  
Civil Engineering, METU

\_\_\_\_\_

Assoc. Prof. Dr. Serdar Göktepe  
Civil Engineering, METU

\_\_\_\_\_

Prof. Dr. Demirkan Çöker  
Aerospace Engineering, METU

\_\_\_\_\_

Assoc. Prof. Dr. Ercan Gürses  
Aerospace Engineering, METU

\_\_\_\_\_

Assoc. Prof. Dr. Hakan Argeşo  
Manufacturing Engineering, Atılım University

\_\_\_\_\_

Date:

**I hereby declare that all information in this document has been obtained and presented in accordance with academic rules and ethical conduct. I also declare that, as required by these rules and conduct, I have fully cited and referenced all material and results that are not original to this work.**

Name, Surname: Berkay Akçören

Signature :

## **ABSTRACT**

### **COMPUTATIONAL MODELING OF RUPTURE IN RUBBERY POLYMERS**

Akçören, Berkay  
M.S., Department of Civil Engineering  
Supervisor: Assoc. Prof. Dr. Serdar Göktepe

January 2020, 68 pages

Rubbery polymers, also known as elastomers, can exhibit large deformations that are generally accompanied by inelastic deformations. Owing to their superior mechanical, physical, and chemical properties, elastomers are widely used in a broad range of industrial applications such as car tires, seismic isolators, mechanical membranes, and seals. For these applications, failure prediction is cardinaly essential. Therefore, this thesis is concerned with the computational failure analysis of rubbery polymers that exhibit highly non-linear material behavior at large deformations. To this end, we model the rupture of rubbery polymers by using the Phase-Field method, where the conservation equation of linear momentum and the evolution equation for the crack phase-field are solved together. While the former describes the mechanical equilibrium, the latter governs damage evolution in rubber. The material behavior of rubbery polymers undergoing damage is modeled by two distinct approaches taken from literature where the damage-induced degradation in the material affects either the entropic and volumetric part of the energy or the energetic and volumetric part of the energy. Moreover, for the entropic elasticity, distinct constitutive approaches are considered. The different modeling approaches are compared through numerical analyses of benchmark problems involving highly heterogeneous deformations of

rubbery polymers undergoing rupture.

**Keywords:** Phase-field method, Fracture, Rubbery polymers

## ÖZ

### LASTİKSİ POLİMERLERDE YIRTIILMANIN HESAPLAMALI MODELLENMESİ

Akçören, Berkay  
Yüksek Lisans, İnşaat Mühendisliği Bölümü  
Tez Yöneticisi: Doç. Dr. Serdar Göktepe

Ocak 2020 , 68 sayfa

Elastomerler olarak da bilinen lastiksi polimerler genellikle elastik olmayan deformasyonları da barındıracak şekilde büyük şekil deęiřtirmeler gösterirler. Üstün mekaniksel, fiziksel ve kimyasal özelliklerinden ötürü, elastomerler araba lastikleri, sismik izolatörler, mekanik membranlar ve contalar gibi endüstriyel uygulamaların oldukça geniş bir yelpazesinde yaygınca kullanılırlar. Bu uygulamalarda hesaplamalı yırtılma kestirimi büyük önem taşır. Bu sebeple, bu tez, büyük deformasyonlarda yüksek derecede doğrusal olmayan malzeme davranışı gösteren lastiksi polimerlerin hesaplamalı yırtılma analizini konu almaktadır. Bu maksatla, lastiksi polimerlerin yırtılmasını doğrusal momentumun korunumu ve çatlak faz alanı deęişim denklemlerinin beraber çözüldüğü Faz Alanı yöntemi kullanarak modellenmiştir. İlk denklem mekanik dengeyi ifade ederken, öbürü kauçuğun hasarını kontrol eder. Hasar gören lastiksi polimerin malzeme davranışı, malzemedeki hasarla azalan bozunmanın enerjinin entropik ve hacimsel kısmını ya da enerjinin enerjik ve hacimsel kısmını etkilediği literatürden alınmış olan iki farklı yaklaşımla modellenmiştir. Ayrıca, entropik elastisite için farklı bünye denklemleri göz önünde bulundurulmuştur. Farklı modelleme yaklaşımları, hasar gören lastiksi polimerlerin heterojen deformasyonlarını içe-

ren referans problemlerinin nümerik analizleri vasıtasıyla kıyaslanmıştır.

**Anahtar Kelimeler:** Faz-alanı yöntemi, Çatlak, Lastiksi polimerler

*To my dearest  
Geran*

## ACKNOWLEDGMENTS

Foremost, I would like to express my appreciation and gratitude to my advisor Dr. Göktepe for his guidance, support, and help throughout my thesis study and graduate life. It is hard to explain his contribution to this thesis and to my personal development. I am indebted to him for sharing all his experience and knowledge with me.

I would like to thank to the members of my thesis examining committee; Dr. Kağan Tuncay, Dr. Ercan Gürses, Dr. Demirkan Çöker and Dr. Hakan Argeşo for their interests on my thesis topic and contributions to this study.

I am grateful to my roommates Sinan Fırat Dal, Onur Solmaz, Bilgin Koçak, Sepehr Seyedian Choubi, Özgür Paşaoğlu, and Dr. Duygu Ergenç for their support and patience during my thesis study.

I would also like to thank a very special person, Baki Aykut Bilginer. He was always with me to overcome all problems. I am very pleased to have him on my side throughout this study.

I would like to thank my family, Şennur Akçören and Ferit Akçören, for their continuous support and encouragement through all my life, particularly my brother, Dinçay Akçören who always inspired me in every aspect of my life.

Finally, I would like to thank my partner in crime; Geran Özdeş Çelik, whose love and support have kept me going on difficult days.

## TABLE OF CONTENTS

ABSTRACT . . . . .	v
ÖZ . . . . .	vii
ACKNOWLEDGMENTS . . . . .	x
TABLE OF CONTENTS . . . . .	xi
LIST OF TABLES . . . . .	xiv
LIST OF FIGURES . . . . .	xv
LIST OF ABBREVIATIONS . . . . .	xviii
CHAPTERS	
1 INTRODUCTION . . . . .	1
1.1 Motivation and Problem Statement . . . . .	1
1.2 Aim and Scope . . . . .	4
1.3 The Outline of the Thesis . . . . .	4
2 FUNDAMENTALS OF CONTINUUM MECHANICS . . . . .	7
2.1 Fundamental Geometric Mappings . . . . .	7
2.2 Length and Area Stretch . . . . .	11
2.3 Concept of Stress and Fundamental Stress Measures . . . . .	12
2.3.1 Cauchy Stress . . . . .	12
2.3.2 Different Stress Measures . . . . .	13

2.4	Balance Principles of Continuum Mechanics . . . . .	15
2.4.1	Balance of Mass . . . . .	15
2.4.2	Balance of Linear Momentum . . . . .	16
2.4.3	Balance of Angular Momentum . . . . .	17
2.4.4	Balance of Energy - First Law of Thermodynamics . . . . .	17
2.4.5	Balance of Entropy - Second Law of Thermodynamics . . . . .	18
3	PHASE FIELD MODELING OF BRITTLE RUPTURE AT FINITE DE- FORMATIONS . . . . .	21
3.1	Geometric derivation of the crack phase-field . . . . .	21
3.2	Extension of Geometric Derivation to Multi-Dimensional Setting . . . . .	23
3.3	Governing Equations of the Coupled Finite Elasticity - Crack Phase- Field Problem . . . . .	24
4	DISCRETIZATION AND FINITE ELEMENT IMPLEMENTATION OF COUPLED PROBLEM . . . . .	27
5	SPECIFICATION OF CONSTITUTIVE MODELS . . . . .	31
5.1	Non-affine Microsphere Model of Hyperelasticity . . . . .	33
5.1.1	Contribution of the Free Chain . . . . .	33
5.1.2	Contribution of the Tube-like Constraint . . . . .	34
5.1.3	Micro-Macro Bridging of State Variables . . . . .	35
5.1.3.1	Free Chain Contribution . . . . .	36
5.1.3.2	Tube Contribution . . . . .	37
5.1.4	Stress and Moduli Expressions . . . . .	37
5.1.5	Integration Over the Sphere . . . . .	40
5.2	Rubber Fracture Model I: Neo-Hookean-type hyperelasticity coupled with Phase-field . . . . .	42

5.3	Rubber fracture model II: Microsphere extension of the bond-stretch model coupled with Phase-field . . . . .	45
5.3.1	Derivation of Stress and Moduli expressions . . . . .	48
5.3.2	Algorithmic update of bond stretch . . . . .	49
6	NUMERICAL RESULTS . . . . .	51
6.1	Discussion of Numerical Results . . . . .	55
7	CONCLUDING REMARKS . . . . .	61
	REFERENCES . . . . .	63

## LIST OF TABLES

### TABLES

Table 2.1	Stress transformation (push-forward / pull-back) rules . . . . .	15
Table 5.1	Material parameters of the Micro-sphere model . . . . .	40
Table 5.2	Integration points with $x$ , $y$ and $z$ coordinates and the associated weights . . . . .	41
Table 5.3	Algorithmic Box for the Microsphere model . . . . .	43
Table 5.4	Material parameters of the Bond-stretch model . . . . .	49
Table 5.5	Iterative Newton scheme for the update of $\lambda_b$ . . . . .	50

## LIST OF FIGURES

### FIGURES

Figure 2.1	Non-linear deformation map $\varphi_t$ maps the material coordinates to spatial coordinates and $\mathbf{F}$ denotes the deformation gradient. . . . .	8
Figure 2.2	Commutative diagram of pull-back and push-forward of metrics. . . . .	10
Figure 2.3	Traction vectors exerted on the material and spatial surfaces of the cut out parts of the body with given unit outward normals . . . . .	12
Figure 2.4	Commutative diagram of pull-back and push-forward of different stress measures. . . . .	13
Figure 3.1	Sharp and diffusive crack modeling. a) Sharp crack b) Diffusive crack with length scale $l$ . . . . .	22
Figure 3.2	Sharp and diffusive crack topology. . . . .	23
Figure 4.1	Staggered solution scheme of the coupled problem. . . . .	30
Figure 5.1	Idealized single chain composed of $N$ Kuhn segments each with length $l$ . . . . .	34
Figure 5.2	a) Kuhn segments are allowed to deform, b) Proposed single chain model. . . . .	46
Figure 6.1	Mesh for penny shaped precracked test specimen and crack region with effective element size $h^e = 0.002$ mm. . . . .	52

Figure 6.2	Load-displacement curves of penny shape precracked test specimens for Rubber Fracture Model I with different element sizes. . . . .	53
Figure 6.3	Penny shaped tension test for Rubber Fracture Model I with element size $h^e = 0.002$ mm. $u_1 = 0$ mm, $u_2 = 0.2$ mm, $u_3 = 0.378$ mm, $u_4 = 0.458$ mm, $u_5 = 0.478$ mm, $u_6 = 0.498$ mm, $u_7 = 0.518$ mm, $u_8 = 0.538$ mm, $u_9 = 0.545$ mm . . . . .	54
Figure 6.4	Corresponding deformed shapes of the specimen for the tension test given in Figure 6.3 . . . . .	55
Figure 6.5	Principal stresses for Fracture Model I with penny shaped precracked test specimen, $u = 0.518$ mm. . . . .	56
Figure 6.6	Mesh for double-notch specimen and crack region. . . . .	57
Figure 6.7	a) Comparison of the numerical results of Rubber Fracture Model I with experimental data in plane-strain solution. b) Comparison of the numerical results of Rubber Fracture Model I with experimental data in plane-stress solution. The chosen material parameters $\mu = 0.203$ N/mm <sup>2</sup> , $\nu = 0.45$ , $g_c = 2.67$ N/mm, $l = 1.0$ mm, $\eta = 1.0 \times 10^{-3}$ mm. . . . .	58
Figure 6.8	Comparison of load-deflection curves for Rubber Fracture Model II from simulations against the experimental results of [1] with chosen material parameters $K = 2.68$ N/mm <sup>2</sup> , $\mu = 0.268$ N/mm <sup>2</sup> , $N = 1000$ , $p = 2.0$ , $\bar{E}_b = 2.67$ N/mm <sup>2</sup> , $\varepsilon^f = 0.235$ N/mm, $l = 1.0$ mm, $\eta = 1.0 \times 10^{-2}$ MPa · s . . . . .	58
Figure 6.9	Load-displacement curve of double-edge-notched tension specimen for Rubber Fracture Model II with initial crack length $a = 16$ mm. $u_a = 0.0$ mm, $u_b = 30.5$ mm, $u_c = 37.0$ mm, $u_d = 37.214$ mm, $u_e = 37.229$ mm, $u_f = 37.239$ mm, $u_g = 37.249$ mm, $u_h = 37.259$ mm, $u_i = 37.261$ mm, $u_j = 37.262$ mm. . . . .	59

Figure 6.10	Comparison of load-deflection curves for Rubber Fracture Model II from simulations against the experimental results of [1] with chosen material parameters $\mu = 0.268 \text{ N/mm}^2$ , $N = 1000$ , $\bar{E}_b = 2.67 \text{ N/mm}^2$ , $K = 2.68 \text{ N/mm}^2$ , $\varepsilon^f = 0.240 \text{ N/mm}$ , $l = 1.0 \text{ mm}$ , $\eta = 1.0 \times 10^{-2} \text{ MPa} \cdot \text{s}$ , $p = 1.47$ . . . . .	59
Figure 6.11	Deformed geometry of double-edge-notched tension specimen for different displacement values given in Figure 6.9. . . . .	60

## LIST OF ABBREVIATIONS

tol	Tolerance
FEM	Finite Element Method
FEAP	Finite Element Analysis Program
PF	Phase-Field
GIT	Gauss Integral Theorem
2D	2 Dimensional
3D	3 Dimensional

# CHAPTER 1

## INTRODUCTION

### 1.1 Motivation and Problem Statement

Rubber has been used since 1850 and has gained an important place in daily life. Today, rubber technology is still being developed, and its application areas are gradually increasing due to its superior properties. Rubber is a widely used material in critical technological applications that range from space vehicles, automobile tires, sealings to seismic isolators, to mention a few. To this end, a sound understanding of the failure mechanism in rubbery polymers and its computational prediction are of cardinal importance. A realistic prediction will contribute to the development of the rubber industry and identify potential problems that may arise, and lead to the tailoring of the microstructure of polymeric materials for applications-specific designs.

The thermomechanical behavior of rubber is highly nonlinear, generally inelastic, and time-dependent. In this thesis, we focus on computational modeling of rupture in rubbery polymers. For this purpose, the finite elasticity of elastomers are extended by using the phase-field fracture models.

Imperfections within the specimen may lead to fracture under increasing load. Damage initiates either in the interior part or on the surface of the material. The theoretical foundations of the classical theory of brittle fracture in solids are outlined in the works of [2, 3, 4]. The study of Griffith and Taylor [2] claims that crack propagates if the energy stored in the material at the macroscale is higher than the surface energy dissipated through the creation of new surfaces. This study able to predict the fracture mechanism at the macroscale. However, such a theory is unable to predict crack initiation. Variational methods based on energy minimization in [5, 6] overcome crack

initiation problem. In these studies, sharp crack discontinuities are approximated with a diffusive crack and it has shown that with a significantly small scale parameter  $l_0$ , a regularized crack surface tends to converges to the surface area of a discontinuous crack. Study of Chen, Wang and Suo [7] states that fracture stretch of the highly stretchable elastomers is insensitive to the depth of cut smaller than the material specific length parameter.

In 1952, Rivlin and Thomas [8] proposed a pioneering work in polymer fracture by considering the macroscopic response. Lake and Thomas [9] were able to explain the experimental observations by a molecular theory, which states that rupture is an energetic process at the microscale originating from the breakage of molecular bonds in the polymer network and has been demonstrated experimentally. Additional dissipative mechanisms around the crack tip are discussed in [10]. Moreover, viscoelastic dissipation around the crack tip, also studied in Kroon [11], and Persson and Brener[12]. Fineberg and Marder [13] discuss unstable crack propagation and complicated crack paths in dynamic fracture by considering the critical energy flux around the crack tip.

For information about the deformation-induced softening effect, also known as the Mullins effect, that accompanies the rupture process, the reader is referred to [14] and references therein. In a recently published experimental study, the Mullins effect exploited as toughening mechanism by introducing the sacrificial bonds [15].

In recent years, the modeling of polymeric gels has gained importance due to the developing biomedical applications. The mechanical response and fracture behavior of polymeric gels have the same baseline modeling aspects of the elastomers due to their micro-level structure, which is composed of crosslinked chain molecules. In literature, there are several devoted studies considering the fracture mechanism of polymeric gels [16, 17, 18]. In the study of [18], the phase-field framework is used to express the loss of the stress-bearing capacity of the polymer network at the macro-scale. The study of [17] shares the same idea of stretchable Kuhn segments in microscale, whereas they treat the swelling phenomena of elastomers by splitting the deformation gradient into swelling and mechanical parts.

Over the past few years, the phase-field approach has been used for modeling complex

crack topology. This approach was firstly used in the pioneering work of Francfort and Marigo [19]. Since that time this approach has been used in various applications of the modeling of fracture at large strains, the thermal effects in fracture, and the healing of elastomers, [20],[21], [22]. In the literature, phase-field models for fracture can be divided into two groups, as small-strain models and large-strain models. The proposed model in [23] with the thermodynamically consistent framework derived from the one-dimensional setup is an example for the former. As an example for the latter, some dedicated works can be considered as rupture of elastomeric materials [20, 24], and the bond stretch model used in the fracture mechanism of a rubber specimen is proposed in [25]. The fracture of solids with anisotropic free energy is studied in [26] by introducing structural tensors for the both the anisotropic geometric regularized crack surface and the anisotropic free energy of the bulk material. Most of the proposed models in literature focus on the two-dimensional problems probably owing to the high computational cost. However, phase-field method can be extended to three-dimensional setting straightforwardly [27]. High computational cost can be restrained by using adaptive mesh refinement methods [28]. The operator-split algorithms proposed in [29] ease the numerical implementation of the crack phase-field models. The phase-field approach to fracture is also extended to ductile fracture in some recent works of [30, 31]. The phase-field approach has garnered great attention by the scientific community since it overcomes some modeling problems like sharp crack discontinuities, and complex crack branching. Also, the use of phase-field makes it possible to be implemented within the general finite element solvers without using interface element formulations, element enrichment strategies, and nodal enrichment strategies. Generally, in order to solve the problem of concern numerically, sufficiently fine mesh resolution gives more accurate results for complex crack patterns without any change in structure of algorithm [20]. For more information about the phase-field method, reader is referred to the comprehensive review article [32].

Many constitutive models for the macroscopic response of the rubbery polymers consider the change in configurational entropy [33, 34, 35], and neglect the energetic effects. Recent study of Talamini, Mao, and Anand [25] splits the response of the polymeric network into entropic and energetic part based on the ideas of [9]. By proposing such a split, they were able to express both the stiffening response due

to the finite extensibility of the polymer chain as well as chain scission due to the internal energy increase.

## **1.2 Aim and Scope**

This thesis is concerned with the computational failure analysis of rubbery polymers that exhibit highly non-linear material behavior at large deformations. To this end, we model the rupture of rubbery polymers by using the Phase-Field method, where the conservation equation of linear momentum and the evolution equation for the crack phase-field are solved together. While the former describes the mechanical equilibrium, the latter governs damage evolution in rubber. The material behavior of rubbery polymers undergoing damage is modeled by two distinct approaches taken from literature where the damage-induced degradation in the material affects either the entropic and volumetric part of the energy or the energetic and volumetric part of the energy. Moreover, for the entropic elasticity, distinct constitutive approaches are considered. The different modeling approaches are compared through numerical analyses of benchmark problems involving highly heterogeneous deformations of rubbery polymers undergoing rupture.

## **1.3 The Outline of the Thesis**

In Chapter 2, the fundamentals of non-linear continuum mechanics and the laws of thermodynamics are presented. The governing differential equations are formulated for a solid body undergoing large deformations. The notation introduced in this chapter is used throughout the thesis.

In Chapter 3, continuous formulation for the crack phase-field problem is derived through the geometric derivation. This derivation is also extended to obtain the two-dimensional setting. Moreover, the governing equations of the coupled finite elasticity - crack phase-field problem are provided.

Chapter 4 is devoted to the finite element discretization of the coupled elasticity - crack phase-field equations.

In Chapter 5, the specific constitutive models are introduced. The stress and moduli expressions for these models are derived for their numerical implementations.

Chapter 6 points out the numerical modeling capabilities of the proposed model. Numerical results are compared with the experimental data obtained from the literature. A convergence analysis is performed for a model problem taken from the literature.

In Chapter 7, concluding remarks regarding the obtained results are given and future work is suggested.



## CHAPTER 2

### FUNDAMENTALS OF CONTINUUM MECHANICS

This chapter outlines the basic concepts of continuum mechanics and the key quantities that constitute governing equations. The kinematics of deformation, stress measures and balance equations will be introduced. The concepts outlined here are broadly studied in literature, and for further reading reader is referred to [36], [37], [38] and [39].

#### 2.1 Fundamental Geometric Mappings

Let *material part*  $B$  be a part of body  $\mathcal{B}$  which is furnished by the *reference* coordinate system  $\mathbf{X} \in \mathbb{R}^3$ . Similarly, *spatial point*  $S_t$  be a part of body  $\mathcal{S}_t$  which is furnished by the *spatial* coordinate system  $\mathbf{x} \in \mathbb{R}^3$ . The former coordinate system lies in the *undeformed* state whereas the latter one lies in the *deformed* state. The relation between *deformed* and *undeformed* states is defined through

$$\varphi_t := \begin{cases} B_t \rightarrow S_t, \\ \mathbf{X} \mapsto \mathbf{x} = \varphi_t(\mathbf{X}) \end{cases} \quad (2.1)$$

the nonlinear deformation map, which maps the undeformed coordinates to deformed coordinates, see Figure 2.1.

Since the deformation map  $\varphi_t(\mathbf{X})$  is bijective, it can be inverted uniquely to obtain the *inverse deformation map*.

$$\varphi_t^{-1} := \begin{cases} S_t \rightarrow B, \\ \mathbf{x} \mapsto \mathbf{X} = \varphi_t^{-1}(\mathbf{x}) \end{cases} \quad (2.2)$$

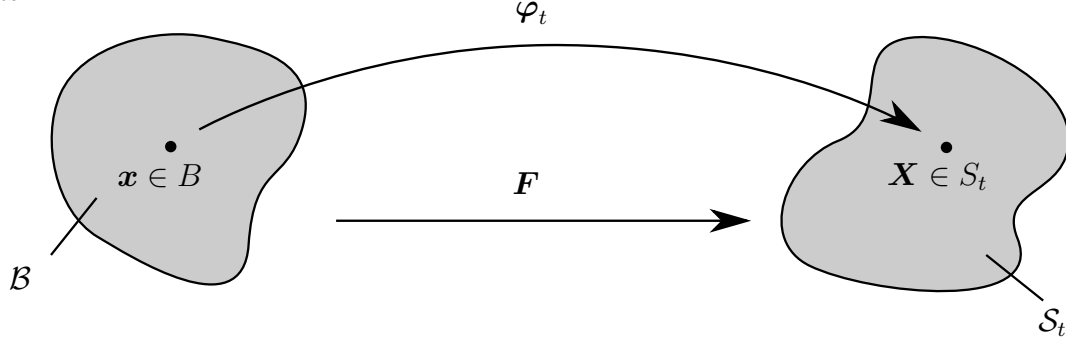


Figure 2.1: Non-linear deformation map  $\varphi_t$  maps the material coordinates to spatial coordinates and  $\mathbf{F}$  denotes the deformation gradient.

The material velocity and acceleration are then defined as

$$\begin{aligned}\mathbf{V}(\mathbf{X}, t) &:= \frac{d}{dt} \varphi_{\mathbf{X}}(t) = \frac{\partial}{\partial t} \varphi(\mathbf{X}, t) \\ \mathbf{A}(\mathbf{X}, t) &:= \frac{d}{dt} \mathbf{V}_{\mathbf{X}}(t) = \frac{\partial}{\partial t} \mathbf{V}(\mathbf{X}, t)\end{aligned}\tag{2.3}$$

The spatial counterparts of  $\mathbf{V}(\mathbf{X}, t)$  and  $\mathbf{A}(\mathbf{X}, t)$  can be obtained by reparametrizing the functional dependency of the fields in terms of current coordinates  $\mathbf{x}$ . The spatial velocity and acceleration are then defined as;

$$\begin{aligned}\mathbf{v}(\mathbf{x}, t) &:= \mathbf{V}(\varphi_t^{-1}(\mathbf{x}), t) = \mathbf{V}_t(\mathbf{X}) \circ \varphi_t^{-1}(\mathbf{x}) \\ \mathbf{a}(\mathbf{x}, t) &:= \mathbf{A}(\varphi_t^{-1}(\mathbf{x}), t) = \mathbf{A}_t(\mathbf{X}) \circ \varphi_t^{-1}(\mathbf{x})\end{aligned}\tag{2.4}$$

Note that both  $\mathbf{V}(\mathbf{X}, t)$  and  $\mathbf{v}(\mathbf{x}, t)$ ;  $\mathbf{A}(\mathbf{X}, t)$  and  $\mathbf{a}(\mathbf{x}, t)$  are same vectors but former ones are parametrized in terms of material coordinates  $\mathbf{X}$ , whereas latter ones are parametrized in terms of the current coordinates  $\mathbf{x}$ .

The *deformation gradient*, the most fundamental deformation measure, can be considered as a linear map of referential tangent vectors  $\mathbf{T} \in T_{\mathbf{X}}\mathcal{B}$  onto the spatial counterparts  $\mathbf{t} \in T_{\mathbf{x}}\mathcal{S}_t$ .

$$\mathbf{F} := \nabla_{\mathbf{X}} \varphi_t(\mathbf{X}) \quad \text{with} \quad F_{aB} = \frac{\partial \varphi_a}{\partial X_B}.\tag{2.5}$$

$$\mathbf{F} := \begin{cases} T_{\mathbf{X}}\mathcal{B} \rightarrow T_{\mathbf{x}}\mathcal{S}_t \\ \mathbf{T} \mapsto \mathbf{t} = \mathbf{F}\mathbf{T} \end{cases}\tag{2.6}$$

The cofactor of the deformation gradient

$$\text{cof } \mathbf{F} := \det \mathbf{F} \mathbf{F}^{-T} = J \mathbf{F}^{-T}, \quad (2.7)$$

where

$$\mathbf{F}^{-T} := \begin{cases} T_X^* \mathcal{B} \rightarrow T_x^* \mathcal{S}, \\ \mathbf{N} \mapsto \mathbf{n} = \mathbf{F}^{-T} \mathbf{N}, \end{cases} \quad (2.8)$$

maps the material normal vectors  $\mathbf{N} \in T_X^* \mathcal{B}$  to the spatial normal vectors  $\mathbf{n} \in T_x^* \mathcal{S}$ .

The volume (*Jacobi*) map is defined through the *Jacobian*,

$$J := \det(\mathbf{F}) \quad \text{and} \quad J = \frac{dv}{dV}, \quad (2.9)$$

with

$$J := \begin{cases} \mathbb{R}_+ \rightarrow \mathbb{R}_+ \\ dV \mapsto dv = J dV \end{cases} \quad (2.10)$$

that transforms the volume element in the reference configuration  $dV$  to the volume element in the current configuration  $dv$ . The value of the *Jacobian* is restricted to the value  $J > 0$  for admissible deformations. A positive *Jacobian* ensures the invertibility of the deformation gradient and impenetrability of a material body.

In order to measure the length quantities in a curved manifold, we define metric tensors as a mapping from tangent to co-tangent spaces.

$$\begin{aligned} \mathbf{G} &: T_X \mathcal{B} \rightarrow T_X^* \mathcal{B}, \\ \mathbf{g} &: T_x \mathcal{S} \rightarrow T_x^* \mathcal{S}. \end{aligned} \quad (2.11)$$

Both metric tensors reduce to Kronecker delta ( $\delta_{ij} = 1$  for  $i = j$ ) in case of the Cartesian coordinate system.

$$\begin{aligned} G_{IJ} &= \delta_{IJ}, \\ g_{ij} &= \delta_{ij}. \end{aligned} \quad (2.12)$$

Having the metrics and the *deformation gradient* defined, we can now interpret the *right Cauchy-Green* and *left Cauchy-Green* deformation tensors as pull-back of the

current metric and push-forward of the inverse reference metric, respectively. *Pull-back* and *push-forward* operations on covariant objects are defined as;

$$\begin{aligned} \blacksquare &= \varphi^*(\bullet) = \mathbf{F}^T (\bullet) \mathbf{F}, \\ \bullet &= \varphi_*(\blacksquare) = \mathbf{F}^{-T} (\blacksquare) \mathbf{F}^{-1}, \end{aligned} \quad (2.13)$$

whereas *pull-back* and *push-forward* operations on contravariant objects are defined as;

$$\begin{aligned} \blacksquare &= \varphi^*(\bullet) = \mathbf{F}^{-1} (\bullet) \mathbf{F}^{-T}, \\ \bullet &= \varphi_*(\blacksquare) = \mathbf{F} (\blacksquare) \mathbf{F}^T, \end{aligned} \quad (2.14)$$

The *right Cauchy-Green* tensor  $\mathbf{C} := \varphi^*(\mathbf{g})$  and its inverse  $\mathbf{C}^{-1} := \varphi_*(\mathbf{g}^{-1})$  are defined by

$$\begin{aligned} \mathbf{C} &:= \varphi^*(\mathbf{g}) = \mathbf{F}^T \mathbf{g} \mathbf{F} & C_{AB} &:= F_{aA} g_{ab} F_{bB} \\ \mathbf{C}^{-1} &:= \varphi_*(\mathbf{g}^{-1}) = \mathbf{F}^{-T} \mathbf{g}^{-1} \mathbf{F}^{-1} & (C^{-1})_{AB} &:= (F^{-1})_{Aa} g_{ab}^{-1} (F^{-1})_{Bb} \end{aligned} \quad (2.15)$$

The *left Cauchy-Green*  $\mathbf{b} := \varphi_*(\mathbf{G}^{-1})$  and its inverse  $\mathbf{b}^{-1} := \varphi_*(\mathbf{G})$  are defined by similarly

$$\begin{aligned} \mathbf{b} &:= \varphi_*(\mathbf{G}^{-1}) = \mathbf{F} \mathbf{G}^{-1} \mathbf{F}^T & b_{ab} &:= F_{aA} G_{AB}^{-1} F_{bB} \\ \mathbf{b}^{-1} &:= \varphi_*(\mathbf{G}) = \mathbf{F}^{-T} \mathbf{G} \mathbf{F}^{-1} & (b^{-1})_{ab} &:= (F^{-1})_{Aa} G_{AB} (F^{-1})_{Bb} \end{aligned} \quad (2.16)$$

The above equations summarized in the commutative diagram, shown in Figure 2.2.

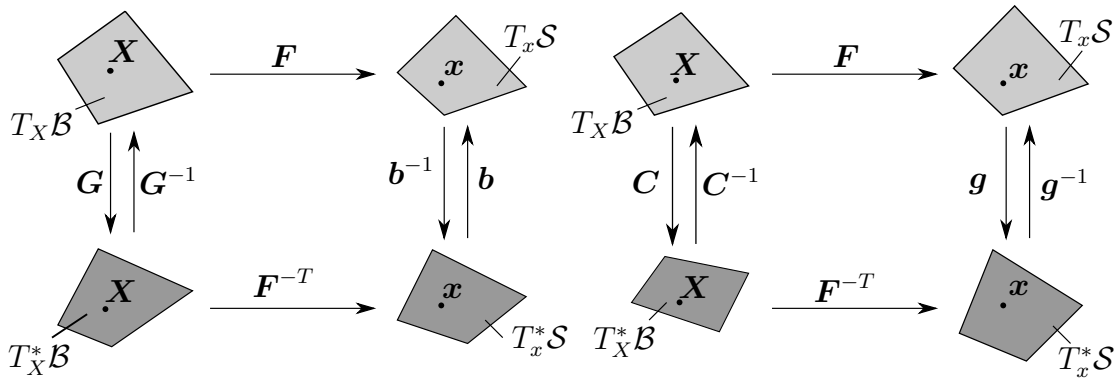


Figure 2.2: Commutative diagram of pull-back and push-forward of metrics.

## 2.2 Length and Area Stretch

The deformation gradient and the deformation tensors play a fundamental role in measuring the basic deformations. To illustrate this, let tangents  $\mathbf{T} \in T_X\mathcal{B}$  and  $\mathbf{t} := \mathbf{F}\mathbf{T} \in T_x\mathcal{S}$  be the undeformed and deformed tangents, respectively. *Stretch*, is defined as the ratio between the length of the deformed tangent  $\mathbf{t}$  and the length of the undeformed tangent  $\mathbf{T}$ , i.e.  $\lambda := \|\mathbf{t}\|_g / \|\mathbf{T}\|_G = \sqrt{\mathbf{t} \cdot \mathbf{g}\mathbf{t}} / \sqrt{\mathbf{T} \cdot \mathbf{G}\mathbf{T}} > 0$ . By setting  $\|\mathbf{T}\|_G = 1$ , the stretch can be obtained as,

$$\begin{aligned} \lambda &= \frac{\sqrt{\mathbf{t} \cdot \mathbf{g}\mathbf{t}}}{1} = \sqrt{\mathbf{F}\mathbf{T} \cdot \mathbf{g}\mathbf{F}\mathbf{T}} \\ &= \sqrt{\mathbf{T} \cdot \mathbf{F}^T \mathbf{g}\mathbf{F}\mathbf{T}} \\ &= \sqrt{\mathbf{T} \cdot \mathbf{C}\mathbf{T}} = \|\mathbf{T}\|_C \end{aligned} \quad (2.17)$$

and by setting  $\|\mathbf{t}\|_g = 1$ , inverse stretch can be obtained as

$$\begin{aligned} \lambda^{-1} &= \frac{\sqrt{\mathbf{T} \cdot \mathbf{G}\mathbf{T}}}{1} = \sqrt{\mathbf{F}^{-1}\mathbf{t} \cdot \mathbf{G}\mathbf{F}^{-1}\mathbf{t}} \\ &= \sqrt{\mathbf{t} \cdot \mathbf{F}^{-T} \mathbf{G}\mathbf{F}^{-1}\mathbf{t}} \\ &= \sqrt{\mathbf{t} \cdot \mathbf{b}^{-1}\mathbf{t}} = \|\mathbf{t}\|_{\mathbf{b}^{-1}}. \end{aligned} \quad (2.18)$$

The metric tensors  $\mathbf{G}$  and  $\mathbf{g}$  can be thought of rulers whose lengths dependent on position. Although the length of the reference tangent  $\mathbf{T}$  does not change,  $\lambda$  changes with deformation, and that deformation information contained in  $\mathbf{C}$ . It can be considered as, the vector in the space remains constant but the ruler which is used to measure the length of the vector changes with time.

Analogous to the length stretch  $\lambda$  defined in (2.18), the *area stretch*,  $\nu$ , is introduced as the ratio of the length of the deformed normal  $\mathbf{n}$  to the length of the undeformed normal  $\mathbf{N}$ , i.e.  $\nu := \|\mathbf{n}\|_{g^{-1}} / \|\mathbf{N}\|_{G^{-1}} = \sqrt{\mathbf{n} \cdot \mathbf{g}^{-1}\mathbf{n}} / \sqrt{\mathbf{N} \cdot \mathbf{G}^{-1}\mathbf{N}} > 0$ . Holding the reference value  $\|\mathbf{N}\|_{G^{-1}} = 1$  the area stretch obtained as

$$\begin{aligned} \nu &= \frac{\|\mathbf{n}\|_{g^{-1}}}{1} = \sqrt{\mathbf{n} \cdot \mathbf{g}^{-1}\mathbf{n}} \\ &= \sqrt{\mathbf{F}^{-T} \mathbf{N} \cdot \mathbf{g}^{-1} \mathbf{F}^{-T} \mathbf{N}} \\ &= \sqrt{\mathbf{N} \cdot \mathbf{F}^{-1} \mathbf{g}^{-1} \mathbf{F}^{-T} \mathbf{N}} = \|\mathbf{N}\|_{C^{-1}} \end{aligned} \quad (2.19)$$

and by setting  $\|\mathbf{n}\|_{g^{-1}} = 1$  inverse area stretch obtained as

$$\begin{aligned}
 \nu^{-1} &= \frac{\|\mathbf{N}\|_{G^{-1}}}{1} = \sqrt{\mathbf{N} \cdot \mathbf{G}^{-1} \mathbf{N}} \\
 &= \sqrt{\mathbf{F}^T \mathbf{n} \cdot \mathbf{G}^{-1} \mathbf{F} \mathbf{n}} \\
 &= \sqrt{\mathbf{n} \cdot \mathbf{F} \mathbf{G}^{-1} \mathbf{F}^T \mathbf{n}} = \|\mathbf{n}\|_b.
 \end{aligned} \tag{2.20}$$

### 2.3 Concept of Stress and Fundamental Stress Measures

Consider a material part  $\mathcal{B}_p \subset \mathcal{B}$  cut off from the reference body  $\mathcal{B}$  and its spatial counterpart  $\mathcal{S}_p \subset \mathcal{S}$  surrounded by boundaries  $\partial\mathcal{B}_p$  and  $\partial\mathcal{S}_p$  with outward unit normals  $\mathbf{N}$  and  $\mathbf{n}$ , respectively as depicted in Figure 2.3.

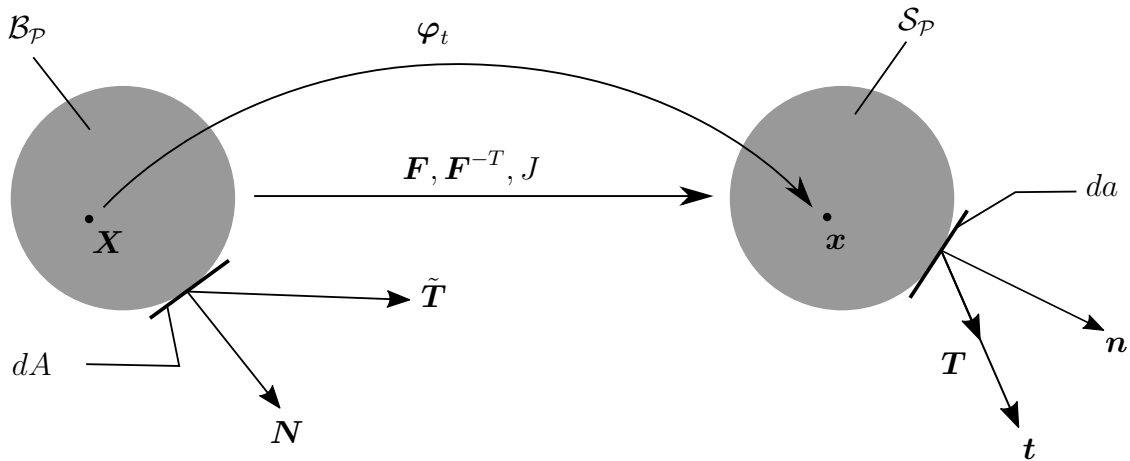


Figure 2.3: Traction vectors exerted on the material and spatial surfaces of the cut out parts of the body with given unit outward normals

#### 2.3.1 Cauchy Stress

Let  $\mathbf{t}$  denote the *Cauchy* (true) stress traction vector exerted on  $da$ , the deformed surface area with unit normal  $\mathbf{n}$ . The *Cauchy stress theorem* states that the spatial traction vector  $\mathbf{t} \in T_x\mathcal{S}$  linearly depends on the spatial normal  $\mathbf{n} \in T_x^*\mathcal{S}$  of the surface  $\partial\mathcal{S}_p$ , through a unique second-order tensor field  $\boldsymbol{\sigma}$  so that

$$\mathbf{t}(\mathbf{x}, t; \mathbf{n}) := \boldsymbol{\sigma}(\mathbf{x}, t) \mathbf{n} \quad \text{with} \quad t_a = \sigma_{ab} n_b. \tag{2.21}$$

From the geometrical viewpoint,  $\sigma$  can be thought as a mapping of normal vectors  $\mathbf{n}$  onto tangent vectors.

$$\sigma := \begin{cases} T_x^* \mathcal{S} & \rightarrow T_x \mathcal{S}, \\ \mathbf{n} & \mapsto \mathbf{t} = \sigma \mathbf{n}. \end{cases} \quad (2.22)$$

An immediate consequence of (2.21) is

$$\mathbf{t}(\mathbf{x}, t; \mathbf{n}) = -\mathbf{t}(\mathbf{x}, t; -\mathbf{n}) \quad (2.23)$$

for all unit normal vectors  $\mathbf{n}$ . This is known as the *Newton's third law*, action and reaction.

### 2.3.2 Different Stress Measures

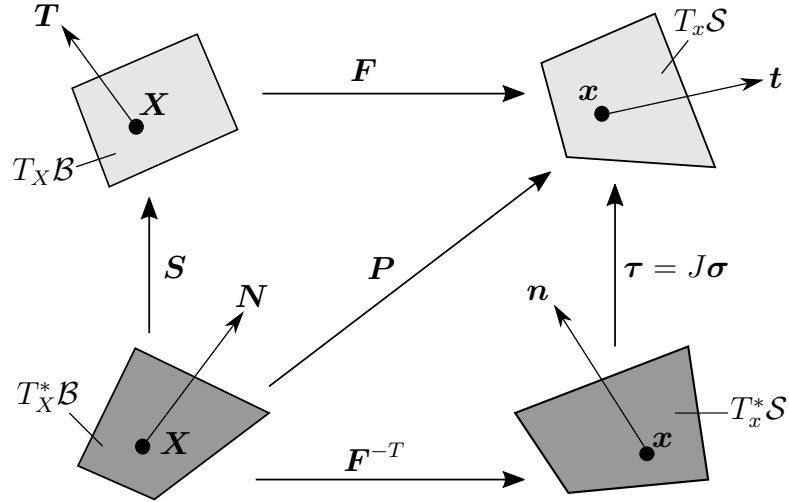


Figure 2.4: Commutative diagram of pull-back and push-forward of different stress measures.

Another spatial stress measure, the *Kirchhoff stress tensor* is obtained by weighting the *Cauchy stress tensor* with the Jacobian

$$\tau := J\sigma, \quad (2.24)$$

also known as the *weighted Cauchy stress tensor*. Another stress tensor defined through the force equality between the deformed and undeformed areas

$$\mathbf{T}dA = \mathbf{t}da. \quad (2.25)$$

Note that, the traction vector  $\mathbf{T}$  is measured per deformed area and  $\mathbf{T}$  and  $\mathbf{t}$  are parallel, see Figure 2.3. By using (2.25) and (2.21), the Lagrangean counterpart of the *Cauchy Theorem* can be constructed.

$$\begin{aligned} \mathbf{P} \mathbf{N} dA &= \boldsymbol{\sigma} \mathbf{n} da, \\ \mathbf{P} &= J \boldsymbol{\sigma} \mathbf{F}^{-T} = \boldsymbol{\tau} \mathbf{F}^{-T}. \end{aligned} \quad (2.26)$$

We introduce the *Nominal Stress tensor*, also known as the *first Piola-Kirchhoff stress tensor*, as a two-point tensor

$$\mathbf{P} := \begin{cases} T_X^* \mathcal{B} & \rightarrow T_x \mathcal{S}, \\ \mathbf{N} & \mapsto \mathbf{T} = \mathbf{P} \mathbf{N}, \end{cases} \quad (2.27)$$

which maps the undeformed normals to deformed tangents. The transformation  $(\blacksquare) = J(\bullet) \mathbf{F}^{-T}$  used in the derivation of the *first Piola stress tensor* is called the *Piola Identity*. It is used for transforming the Lagrangean equations to Eulerian equations. The immediate outcome of the Piola transformation is the Piola Identity

$$J \operatorname{div}(\bullet) = \operatorname{DIV}(\blacksquare) = \operatorname{DIV}(J(\bullet) \mathbf{F}^{-T}) \quad (2.28)$$

where  $(\blacksquare)$  defined as a Lagrangean object, whereas  $(\bullet)$  defines an Eulerian object. The last stress measure, the *second Piola-Kirchhoff stress tensor*, is defined through  $\tilde{\mathbf{T}} = \mathbf{S} \mathbf{N}$

$$\mathbf{S} := \begin{cases} T_X^* \mathcal{B} & \rightarrow T_X \mathcal{B}, \\ \mathbf{N} & \mapsto \tilde{\mathbf{T}} = \mathbf{S} \mathbf{N}, \end{cases} \quad (2.29)$$

where  $\tilde{\mathbf{T}} := \mathbf{F}^{-1} \mathbf{T} \in T_X \mathcal{B}$ .

Note that the *first Piola-Kirchhoff stress tensor* can be interpreted as the *engineering stress tensor* and the *Cauchy stress tensor* as the *true stress tensor*.

Incorporating the equations (2.24), (2.26), and (2.29) all stress measures can be expressed in terms of each other by applying the pull-back and push-forward operations.

$$\begin{aligned} \boldsymbol{\tau} &= \mathbf{P} \mathbf{F}^T &= \mathbf{F} \mathbf{S} \mathbf{F}^T \\ \mathbf{P} &= \boldsymbol{\tau} \mathbf{F}^{-T} &= \mathbf{F} \mathbf{S} \\ \mathbf{S} &= \mathbf{F}^{-1} \mathbf{P} &= \mathbf{F}^{-1} \boldsymbol{\tau} \mathbf{F}^{-T} \end{aligned} \quad (2.30)$$

These transformations are summarized in the commutative diagram given in Figure 2.4 and Table 2.1.

Table 2.1: Stress transformation (push-forward / pull-back) rules

	$\boldsymbol{\sigma}$	$\boldsymbol{\tau}$	$\boldsymbol{P}$	$\boldsymbol{S}$
$\boldsymbol{\sigma} =$	$\boldsymbol{\sigma}$	$J^{-1}\boldsymbol{\tau}$	$J^{-1}\boldsymbol{P}\boldsymbol{F}^T$	$J^{-1}\boldsymbol{F}\boldsymbol{S}\boldsymbol{F}^T$
$\boldsymbol{\tau} =$	$J\boldsymbol{\sigma}$	$\boldsymbol{\tau}$	$\boldsymbol{P}\boldsymbol{F}^T$	$\boldsymbol{F}\boldsymbol{S}\boldsymbol{F}^T$
$\boldsymbol{P} =$	$J\boldsymbol{\sigma}\boldsymbol{F}^{-T}$	$\boldsymbol{\tau}\boldsymbol{F}^{-T}$	$\boldsymbol{P}$	$\boldsymbol{F}\boldsymbol{S}$
$\boldsymbol{S} =$	$J\boldsymbol{F}^{-1}\boldsymbol{\sigma}\boldsymbol{F}^{-T}$	$\boldsymbol{F}^{-1}\boldsymbol{\tau}\boldsymbol{F}^{-T}$	$\boldsymbol{F}^{-1}\boldsymbol{P}$	$\boldsymbol{S}$

## 2.4 Balance Principles of Continuum Mechanics

The balance laws of continuum mechanics are a set of differential equations that must be valid and satisfied by any material for all times. The solution of these differential equations with proper initial and boundary conditions provides us with the primary variables. For this purpose, we derive the local form for the balance laws, which are initially written in the integral form. In order to obtain their local form, first, the Gauss integral theorem (GIT) is used to transform the flux terms on the surface integrals, and localization is applied for vanishing infinitesimal body point.

### 2.4.1 Balance of Mass

Let  $\mathcal{S}_p \subset \mathcal{S}$  is a cut out part of  $\mathcal{S}$ , with its Lagrangean counterpart  $\mathcal{B}_p \subset \mathcal{B}$ . In a closed system, where there exists no mass sources or mass flux, we assume that mass cannot be produced or destroyed. Therefore, the mass of the cut out body is conserved.

$$\frac{d}{dt}(\mathcal{M}_{\mathcal{S}_p}) = \frac{d}{dt} \int_{\mathcal{S}_p} \rho \, dv = \frac{d}{dt} \int_{\mathcal{B}_p} \rho J \, dV = \frac{d}{dt} \int_{\mathcal{B}_p} \rho_0 \, dV = 0 \quad (2.31)$$

where  $\rho(\boldsymbol{x}, t)$  is the *spatial mass density* and  $\rho_0(\boldsymbol{X})$  is the *reference mass density*. This equation must hold locally. Therefore  $(\rho J - \rho_0) = 0 \rightarrow \rho J = \rho_0$ . Since body part  $\mathcal{B}_p$  does not change over time, we can rewrite the third expression in (2.31)

$$\int_{\mathcal{B}_p} (\dot{\rho} J + \rho \dot{J}) \, dV = 0 \quad (2.32)$$

for vanishing part  $\lim \mathcal{B}_p \rightarrow 0$  and  $\dot{J} = J \operatorname{div} \mathbf{v}$ . The local form of the mass balance equation is acquired as

$$\dot{\rho} + \rho \operatorname{div} \mathbf{v} = 0 \quad \text{and} \quad \rho_0(\mathbf{X}) = \rho(\mathbf{x}, t) J(\mathbf{x}, t) \quad (2.33)$$

where the former one is in the *spatial setting* while the latter one is in the *material setting*.

## 2.4.2 Balance of Linear Momentum

The balance of linear momentum states that the temporal change of linear momentum  $\mathcal{I}_{S_p}$  of  $S_p \subset \mathcal{S}$  is equal to the sum of the forces  $\mathcal{F}_{S_p}$  acting on the  $S_p$ .

$$\frac{d}{dt} \left( \mathcal{I}_{S_p} \right) = \mathcal{F}_{S_p} \quad (2.34)$$

where  $\mathcal{I}_{S_p}$  and  $\mathcal{F}_{S_p}$  defined as

$$\begin{aligned} \mathcal{I}_{S_p} &= \int_{S_p} \rho \mathbf{v} \, dv, \\ \mathcal{F}_{S_p} &= \underbrace{\int_{S_p} \rho \mathbf{b} \, dv}_{\text{body forces}} + \underbrace{\int_{\partial S_p} \mathbf{t} \, da}_{\text{surface forces}}. \end{aligned} \quad (2.35)$$

Combining equations (2.34) and (2.35), we arrive at

$$\underbrace{\frac{d}{dt} \int_{S_p} \rho \mathbf{v} \, dv}_{\text{A}} = \int_{S_p} \rho \mathbf{b} \, dv + \underbrace{\int_{\partial S_p} \mathbf{t} \, da}_{\text{B}} \quad (2.36)$$

Terms A and B are treated separately; that is,

$$\text{A} \quad \frac{d}{dt} \int_{S_p} \rho \mathbf{v} \, dv = \int_{S_p} \rho \dot{\mathbf{v}} \, dv + \int_{S_p} \mathbf{v} \underbrace{\frac{d}{dt} (\rho \, dv)}_{= 0 \text{ due to (2.31)}} \quad (2.37)$$

$$\text{B} \quad \int_{\partial S_p} \mathbf{t} \, da \stackrel{(2.22)}{=} \int_{\partial S_p} \boldsymbol{\sigma} \mathbf{n} \, da \stackrel{(GIT)}{=} \int_{S_p} \operatorname{div}(\boldsymbol{\sigma}) \, dv \quad (2.38)$$

Combining equations (2.36-2.38), we obtain

$$\int_{S_p} \rho \dot{\mathbf{v}} \, dv = \int_{S_p} \operatorname{div}(\boldsymbol{\sigma}) \, dv + \int_{S_p} \rho \mathbf{b} \, dv. \quad (2.39)$$

The localization of (2.39) results in

$$\rho \dot{\mathbf{v}} = \operatorname{div}(\boldsymbol{\sigma}) + \rho \mathbf{b} \quad (2.40)$$

Recalling  $\mathbf{a} = \dot{\mathbf{v}} = \frac{d}{dt} \mathbf{v}$  and by using (2.24) above expression is rearranged as

$$\rho \mathbf{a} = \operatorname{div}(J^{-1} \boldsymbol{\tau}) + \rho \mathbf{b} \quad (2.41)$$

In elementary particle mechanics, the well-known equation for the balance of linear momentum appeared as  $\mathbf{F} = m\mathbf{a}$ , also known as the *Newton's Second Law of motion*.

### 2.4.3 Balance of Angular Momentum

The time change of angular momentum of  $\mathcal{S}_P$  is equal to the total moment generated by the external forces; that is,

$$\frac{d}{dt} \int_{\mathcal{S}_P} \mathbf{x} \times \rho \mathbf{v} \, dv = \int_{\mathcal{S}_P} \mathbf{x} \times \rho \mathbf{b} \, dv + \int_{\partial \mathcal{S}_P} \mathbf{x} \times \mathbf{t} \, da \quad (2.42)$$

Exploiting the mass balance (2.31), the equality  $\mathbf{v} \times \mathbf{v} = \mathbf{0}$ , and the Cauchy stress definition (2.22) through the *Gauss integral theorem* we obtain

$$\int_{\mathcal{S}_P} \mathbf{x} \times (\rho \dot{\mathbf{v}} - \rho \mathbf{b} - \operatorname{div}(\boldsymbol{\sigma})) \, dv = \int_{\mathcal{S}_P} \epsilon_{abc} \sigma_{cb} \, dv = \mathbf{0}, \quad (2.43)$$

which is fulfilled only when the Cauchy stresses is symmetric. Thus, the balance of the angular momentum results in

$$\boldsymbol{\sigma} = \boldsymbol{\sigma}^T, \quad (2.44)$$

As a result of the above equality other stress measures are required to satisfy the following symmetry relations.

$$\boldsymbol{\tau} = \boldsymbol{\tau}^T, \quad \mathbf{P}\mathbf{F}^T = \mathbf{F}\mathbf{P}^T, \quad \mathbf{S} = \mathbf{S}^T. \quad (2.45)$$

### 2.4.4 Balance of Energy - First Law of Thermodynamics

This fundamental balance principle states that the rate of the total energy of the body  $\dot{\mathcal{K}} + \dot{\mathcal{U}}$  is equal to the sum of the thermal power  $\mathcal{Q}$  and mechanical power  $\mathcal{P}$ .

$$\dot{\mathcal{K}} + \dot{\mathcal{U}} = \mathcal{P} + \mathcal{Q} \quad (2.46)$$

where the kinetic energy, the internal energy, the mechanical power and the thermal power are defined as

$$\begin{aligned}
\mathcal{P} &= \int_{\mathcal{S}_p} \rho \mathbf{b} \cdot \mathbf{v} \, dv + \int_{\partial \mathcal{S}_p} \mathbf{t} \cdot \mathbf{v} \, da \\
\mathcal{Q} &= - \int_{\mathcal{S}_p} \operatorname{div} \mathbf{q} \, dv + \int_{\mathcal{S}_p} \rho r \, dv \\
\mathcal{K} &= \int_{\mathcal{S}_p} \frac{1}{2} \rho \mathbf{v} \cdot \mathbf{v} \, dv \\
\mathcal{U} &= \int_{\mathcal{S}_p} \rho e \, dv
\end{aligned} \tag{2.47}$$

in terms of the internal heat source  $r$ , the outward heat flux vector  $\mathbf{q}$ , and the internal energy density  $e$ . Combining above definitions, we end up with

$$\int_{\mathcal{S}_p} (\rho \dot{e} + \operatorname{div} \mathbf{q} - \boldsymbol{\sigma} : \mathbf{d} + \rho r) \, dv \tag{2.48}$$

With vanishing part  $\lim \mathcal{B}_p \rightarrow 0$ , local form of the energy balance becomes

$$\rho \dot{e} + \operatorname{div} \mathbf{q} - \boldsymbol{\sigma} : \mathbf{d} + \rho r = 0. \tag{2.49}$$

By multiplying above equation by  $J$  and using the Piola-identity, we get

$$\rho_0 \dot{e} + \operatorname{Div} \mathbf{Q} - \boldsymbol{\tau} : \mathbf{d} + \rho_0 R = 0 \tag{2.50}$$

where  $\mathbf{Q}$  and  $R$  are defined as Eulerian heat flux and Eulerian heat source term.

### 2.4.5 Balance of Entropy - Second Law of Thermodynamics

The entropy of a system can be considered as a measure of disorder. The second law of thermodynamics is an inequality that restricts every process that the entropy production rate of the system must be non-negative. This restriction defines the evolution of every dissipative process. For the part of body  $\mathcal{S}_p$  the total rate of entropy production  $\Gamma$  is defined as

$$\begin{aligned}
\Gamma &= \int_{\mathcal{S}_p} \rho \gamma \, dv = \dot{\mathcal{H}} - \dot{\mathcal{S}} \geq 0 \\
&= \frac{d}{dt} \int_{\mathcal{S}_p} \rho \eta \, dv - \int_{\mathcal{S}_p} \frac{\rho r}{\theta} \, dv + \int_{\mathcal{S}_p} \frac{\mathbf{q} \cdot \mathbf{n}}{\theta} \, da \geq 0
\end{aligned} \tag{2.51}$$

where we introduced  $\gamma$  as the mass-specific spatial rate of entropy production,  $\theta$  as the absolute temperature,  $\eta$  as the mass-specific spatial entropy,  $\mathcal{H}$  as the total entropy of the system, and  $\dot{\mathcal{S}}$  as the total entropy input to the system.

Following the conventional steps, we end up with the local form of the spatial entropy balance

$$\rho\gamma = \rho\dot{\eta} - \frac{1}{\theta}\rho r + \frac{1}{\theta}\operatorname{div} \mathbf{q} - \frac{1}{\theta^2}\mathbf{q} \cdot \nabla_x \theta \geq 0 \quad (2.52)$$

Alternatively, the *Clasius-Duhem Inequality* is expressed as

$$\rho\theta\gamma = \rho\dot{\eta} - (\rho\dot{e} - \boldsymbol{\sigma} : \mathbf{d}) - \frac{1}{\theta}\mathbf{q} \cdot \nabla_x \theta \geq 0 \quad (2.53)$$

where we introduce the dissipation per unit mass as

$$\rho\mathcal{D} := \rho\theta\gamma \geq 0. \quad (2.54)$$

We decompose (2.54) into the *local* and *conductive* parts

$$\rho\mathcal{D} = \rho\mathcal{D}_{loc} + \rho\mathcal{D}_{con} \quad (2.55)$$

and require separately their non-negativeness

$$\begin{aligned} \rho\mathcal{D}_{loc} &:= \boldsymbol{\sigma} : \mathbf{d} - \rho\dot{e} + \rho\theta\dot{\eta} \geq 0 \\ \rho\mathcal{D}_{con} &:= -\frac{1}{\theta}\mathbf{q} \cdot \nabla_x \theta \geq 0 \end{aligned} \quad (2.56)$$

In solid mechanics, it is common to use the *Helmholtz free energy* as a thermodynamic potential. The Helmholtz free energy is defined through the *Legendre transformation*. For more information about the *Legendre transformation* between the thermodynamic potentials, reader is referred to [40]

$$\Psi := e - \theta\eta \quad (2.57)$$

Insertion of (2.57) into the first inequality of (2.56) and multiplying both sides with  $J$  yields,

$$\rho_0\mathcal{D}_{loc} = \boldsymbol{\tau} : \frac{1}{2}\boldsymbol{\mathcal{L}}_v\mathbf{g} - \rho_0\dot{\Psi} \quad (2.58)$$

for isothermal ( $\dot{\theta} = 0$ ) and purely elastic processes ( $\mathcal{D}_{loc} = 0$ ), where  $\mathbf{d} = \frac{1}{2}\boldsymbol{\mathcal{L}}_v\mathbf{g}$ . Therefore, the Coleman's exploitation method implies the following equality.

$$\boldsymbol{\tau} - \rho_0 2\partial_g \Psi = 0 \quad \rightarrow \quad \boldsymbol{\tau} = \rho_0 2\partial_g \Psi, \quad (2.59)$$

which is known as the Doyle-Ericksen formula.



## CHAPTER 3

### PHASE FIELD MODELING OF BRITTLE RUPTURE AT FINITE DEFORMATIONS

This chapter summarizes the derivation of the governing differential equations of phase-field modeling of fracture at finite strains by following the similar steps in [20],[23] and [29]. First, the equation of the phase-field method is derived through the purely geometric approach. Second, the proposed crack regularization function extended to the multi-dimensional setting. Last, the Euler-Lagrange equations of the coupled problem will be derived through the energy balance.

#### 3.1 Geometric derivation of the crack phase-field

Consider a one-dimensional bar with cross-section  $\Gamma$ , which is infinitely long. The bar is lying on the  $x$ -axis and fully cracked in the middle, see Figure 3.1a. The crack condition is characterized by the variable  $d$ .

$$d(x) := \begin{cases} 1 & \text{for } x = 0, \\ 0 & \text{otherwise,} \end{cases} \quad (3.1)$$

where  $d = 1$  indicates the fully broken state whereas  $d = 0$  describes the intact state. We approximate the sharp crack topology with the help of the *length scale* parameter  $l$  by the following function, see Figure 3.1b,

$$d(x) = e^{(-|x|/l)}. \quad (3.2)$$

Notice that, Equation (3.2) is the solution of the following differential equation.

$$d(x) - l^2 d''(x) = 0 \quad \text{and} \quad d(\pm\infty) = 0 \quad (3.3)$$

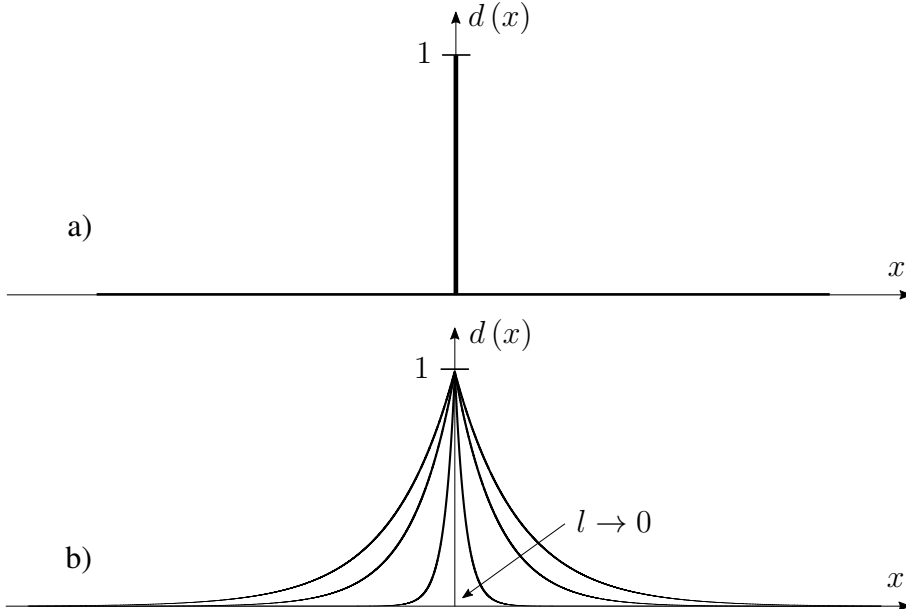


Figure 3.1: Sharp and diffusive crack modeling. a) Sharp crack b) Diffusive crack with length scale  $l$

with the boundary condition  $d(0) = 1$ . This differential equation is non other than the Euler-Lagrange equation of the following minimization problem.

$$d = \inf_{d \in W} I(d) \quad \text{with} \quad W = \{d | d(0) = 1, d(\pm\infty) = 0\} \quad (3.4)$$

where the function  $I(d)$  is defined as,

$$I(d) = \frac{1}{2} \int_B \left\{ d^2 + l^2 d'^2 \right\} dV. \quad (3.5)$$

Substituting Equation (3.2) into (3.5) and transforming the volume integral into the line integral  $dV = \Gamma dx$ , we end up with

$$I(d(x) = e^{(-|x|/l)}) = \Gamma l. \quad (3.6)$$

Therefore, the crack surface can be expressed as,

$$\Gamma_l = \Gamma = \frac{1}{l} I(d) = \frac{1}{2l} \int_B \left\{ d^2 + l^2 d'^2 \right\} dV. \quad (3.7)$$

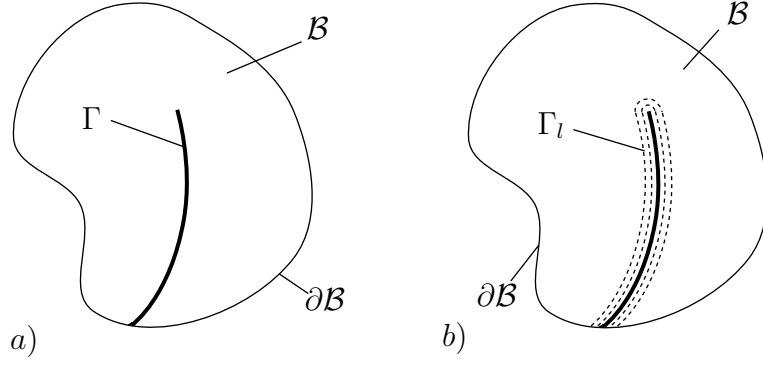


Figure 3.2: Sharp and diffusive crack topology.

### 3.2 Extension of Geometric Derivation to Multi-Dimensional Setting

Let material body  $\mathcal{B}$  occupy a place in  $\delta \in [1, 2, 3]$  dimensional space. We apply a similar procedure and characterize the cracking condition by the variable  $d$ ,

$$d(\mathbf{X}) := \begin{cases} \mathcal{B} \rightarrow [0, 1], \\ \mathbf{X} \rightarrow d(\mathbf{X}) \end{cases} \quad (3.8)$$

inside the solid body  $\mathcal{B}$  in the reference configuration. The sharp crack topology is then approximated by a multi-dimensional extension of Equation (3.7) which is called the *regularized crack surface* by changing the derivative terms to spatial gradient terms  $d' \approx \nabla_{\mathbf{X}} d$ .

$$\Gamma_l := \int_{\mathcal{B}} \gamma(d, \nabla_{\mathbf{X}} d) = \int_{\mathcal{B}} \left\{ \frac{1}{2l} d^2 + \frac{l}{2} |\nabla_{\mathbf{X}} d|^2 \right\} dV. \quad (3.9)$$

Minimization of the above equation gives us the governing differential equation and the necessary boundary conditions of the pure phase-field problem.

$$d - l^2 \Delta d = 0 \quad \text{in } \mathcal{B} \quad \text{and} \quad \nabla_{\mathbf{X}} d \cdot \mathbf{N} = 0 \quad \text{on } \partial \mathcal{B}, \quad (3.10)$$

where  $\Delta d := \text{Div}(\nabla_{\mathbf{X}} d)$ . Notice that the regularized crack surface converges to the sharp crack surface  $\Gamma_l \rightarrow \Gamma$  as the length scale parameter approaches to zero  $l \rightarrow 0$ , see Figure 3.2b.

### 3.3 Governing Equations of the Coupled Finite Elasticity - Crack Phase-Field Problem

We will extend the conservation of energy by adding the damage variable to the bulk free energy and the energy dissipated by the fracture surface by following the similar steps in [25],[23] and [29]. The global energy storage functional of the material body  $\mathcal{B}$  that depends on the field variables  $(\boldsymbol{\varphi}, d)$  is expressed as

$$E(\boldsymbol{\varphi}, d) = \int_{\mathcal{B}} \Psi(\mathbf{F}, d) dV, \quad (3.11)$$

and the rate of the stored free energy for a given state is

$$\mathcal{E}(\dot{\boldsymbol{\varphi}}, \dot{d}; \boldsymbol{\varphi}, d) = \frac{\partial}{\partial t} E(\boldsymbol{\varphi}, d) = \int_{\mathcal{B}} [\mathbf{P} : \dot{\mathbf{F}} + \beta \dot{d}] dV. \quad (3.12)$$

where the nominal stress tensor and crack driving force are defined as  $\mathbf{P} = \partial_{\mathbf{F}} \Psi$  and  $\beta = \partial_d \Psi$  respectively. The externally applied mechanical power is given as

$$\mathcal{P}_{ext} = \int_{\partial \mathcal{B}} \mathbf{T} \cdot \mathbf{V} dA + \int_{\mathcal{B}} \rho_0 \mathbf{B} \cdot \mathbf{V} dV, \quad (3.13)$$

and the energy dissipated by the fracture is given as

$$\mathcal{D} = \int_{\mathcal{B}} g_c \dot{\gamma} dV = \int_{\mathcal{B}} g_c [\partial_d \gamma \dot{d} + \partial_{\nabla_x d} \gamma \nabla_x \dot{d}] dV \quad (3.14)$$

where  $g_c$  is identified as the Griffith-type critical fracture energy parameter. In a system, the external power input should be equal to the rate of energy stored in the system plus dissipation.

$$\begin{aligned} \mathcal{P}_{ext} &= \mathcal{E} + \mathcal{D} \\ \int_{\partial \mathcal{B}} \mathbf{T} \cdot \mathbf{V} dA + \int_{\mathcal{B}} \rho_0 \mathbf{B} \cdot \mathbf{V} dV &= \int_{\mathcal{B}} \underbrace{[\mathbf{P} : \dot{\mathbf{F}} + \beta \dot{d}]}_{\text{(A)}} dV + \int_{\mathcal{B}} \underbrace{[\partial_d \gamma \dot{d} + \partial_{\nabla_x d} \gamma \nabla_x \dot{d}]}_{\text{(B)}} dV. \end{aligned} \quad (3.15)$$

We apply the *divergence theorem* and the *Gauss integral theorem* to the terms denoted as (A) and (B).

$$\begin{aligned} \text{(A)} \quad \int_{\mathcal{B}} \mathbf{P} : \dot{\mathbf{F}} dV &= \int_{\mathcal{B}} \text{Div}(\mathbf{V} \cdot \mathbf{P}) dV - \int_{\mathcal{B}} \text{Div}(\mathbf{P}) \cdot \mathbf{V} dV \\ &= \int_{\partial \mathcal{B}} \mathbf{P} \mathbf{N} \cdot \mathbf{V} dA - \int_{\mathcal{B}} \text{Div}(\mathbf{P}) \cdot \mathbf{V} dV, \end{aligned} \quad (3.16)$$

$$\textcircled{\mathbf{B}} \quad \int_{\mathcal{B}} \partial_{\nabla_x d} \gamma \nabla_x \dot{d} dV = - \int_{\mathcal{B}} \text{Div} (\partial_{\nabla_x d} \gamma) \dot{d} dV + \int_{\mathcal{B}} \partial_{\nabla_x d} \gamma \cdot \mathbf{N} \dot{d} dA. \quad (3.17)$$

Combining equations (3.15)-(3.17) we come up with the final expression

$$\begin{aligned} \int_{\partial \mathcal{B}} \mathbf{T} \cdot \mathbf{V} dA + \int_{\mathcal{B}} \rho_0 \mathbf{B} \mathbf{V} dV &= \int_{\partial \mathcal{B}} \mathbf{P} \mathbf{N} \cdot \mathbf{V} dA - \int_{\mathcal{B}} \text{Div} (\mathbf{P}) \cdot \mathbf{V} dV \\ &+ \int_{\mathcal{B}} \beta \dot{d} dV + \int_{\mathcal{B}} \partial_d \gamma \dot{d} dV \\ &- \int_{\mathcal{B}} \text{Div} (\partial_{\nabla_x d} \gamma) \dot{d} dV + \int_{\mathcal{B}} \partial_{\nabla_x d} \gamma \cdot \mathbf{N} \dot{d} dA. \end{aligned} \quad (3.18)$$

Rearranging the volume and surface integral terms, we arrive at

$$\begin{aligned} \int_{\mathcal{B}} \mathbf{V} \cdot \left( \mathbf{T} - \mathbf{P} \mathbf{N} \right) dA + \int_{\mathcal{B}} \left( \rho_0 \mathbf{B} + \text{Div} (\mathbf{P}) \right) \cdot \mathbf{V} dV \\ + \int_{\mathcal{B}} \left( \text{Div} \partial_{\nabla_x d} \gamma - \beta \right) \dot{d} dV - \int_{\mathcal{B}} \partial_{\nabla_x d} \gamma \cdot \mathbf{N} dA = 0 \end{aligned} \quad (3.19)$$

Since Equation (3.19) must hold for arbitrary rates  $\mathbf{V}$  and  $\dot{d}$ , the Euler Lagrange equations of the coupled problem are obtained as

$$\begin{aligned} \text{Div} \mathbf{Q} - \beta - f &= 0 \text{ in } \mathcal{B}, \\ \text{Div} \mathbf{P} + \rho_0 \mathbf{B} &= \mathbf{0} \text{ in } \mathcal{B}, \\ \mathbf{Q} \cdot \mathbf{N} &= \mathbf{0} \text{ on } \partial \mathcal{B}, \\ \mathbf{T} &= \mathbf{P} \mathbf{N} \text{ on } \partial \mathcal{B}. \end{aligned} \quad (3.20)$$

where we define  $\mathbf{Q} = \partial_{\nabla_x d} \gamma$  and  $f = \partial_d \gamma$ . The Eulerian versions of the above equations are given as

$$\begin{aligned} J \text{div} \mathbf{q} - \beta - f &= 0 \text{ in } \mathcal{B}, \\ \text{div} \boldsymbol{\sigma} + \rho \mathbf{b} &= \mathbf{0} \text{ in } \mathcal{S}, \end{aligned} \quad (3.21)$$

with body force  $\mathbf{b}$  and the Cauchy stress tensor  $\boldsymbol{\sigma}$ .  $\mathbf{q}$  is calculated from the Piola-Identity (2.28).

$$J \text{div} \mathbf{q} = \text{Div} \mathbf{Q} \quad \text{with} \quad \mathbf{Q} = J \mathbf{q} \mathbf{F}^{-T} \quad (3.22)$$



## CHAPTER 4

### DISCRETIZATION AND FINITE ELEMENT IMPLEMENTATION OF COUPLED PROBLEM

This chapter outlines the solution technique for the derived coupled problem (3.20) with the corresponding boundary conditions (3.20). Since those equations are impossible to solve analytically for complex geometries, the solution is obtained approximately by using the finite element method. For further details about the finite element implementation reader is referred to [41, 42].

First, the weak forms of the coupled differential equations will be constructed through the Galerkin method. We multiply the both equations with the corresponding test functions ( $\varphi^* \in \mathcal{U}$ ) and ( $d^* \in \mathcal{V}$ ) which conforms the homogeneous boundary conditions ( $\varphi^* = 0$  on  $\partial\mathcal{B}_\varphi$ ) and ( $d^* = 0$  on  $\partial\mathcal{B}_d$ ) and integrate over the body.

$$\begin{aligned} G^\varphi(\varphi, \varphi^*; d) &= G_{\text{int}}^\varphi(\varphi, \varphi^*; d) - G_{\text{ext}}^\varphi(\varphi, \varphi^*; d) \\ G^d(d, d^*; \varphi) &= G_{\text{int}}^d(d, d^*; \varphi) - G_{\text{ext}}^d(d, d^*; \varphi) \end{aligned} \quad (4.1)$$

where the internal and external Galerkin functionals for the balance laws are obtained as,

$$\begin{aligned} G_{\text{int}}^\varphi(\varphi, \varphi^*; d) &= \int_{\mathcal{B}} \nabla_x \varphi^* : \boldsymbol{\tau} \, dV \\ G_{\text{ext}}^\varphi(\varphi, \varphi^*; d) &= \int_{\mathcal{B}} \rho \varphi^* \cdot \mathbf{B} \, dV + \int_{\partial\mathcal{B}_T} \varphi^* \cdot \mathbf{T} \, dA \\ G_{\text{int}}^d(d, d^*; \varphi) &= \int_{\mathcal{B}} \nabla_x d^* \cdot \hat{\mathbf{q}} \, dV + \int_{\mathcal{B}} d^* \beta \, dV + \int_{\mathcal{B}} d^* f \, dV \\ G_{\text{ext}}^d(d, d^*; \varphi) &= \int_{\partial\mathcal{B}_d} d^* \mathbf{Q} \cdot \mathbf{N} \, dA = \mathbf{0} \quad \text{due to (3.20)}. \end{aligned} \quad (4.2)$$

Here,  $\mathbf{B}$  is defined as a body force,  $\mathbf{T}$  as surface traction vector. The external Galerkin functional for the damage problem vanishes identically due to the boundary condition (3.20). Since Galerkin functionals are nonlinear functions of the solution fields, they

need to be linearized. The linearization around  $\bar{\varphi}$ ,  $\bar{d}$  with the incremental terms  $\hat{\varphi} = \varphi - \bar{\varphi}$  and  $\hat{d} = d - \bar{d}$  results in,

$$\begin{aligned}\text{Lin } G^\varphi(\varphi, \varphi^*; d)|_{\bar{\varphi}, \bar{d}} &:= G^\varphi(\bar{\varphi}, \varphi^*; \bar{d}) + \Delta G^\varphi(\varphi, \varphi^*, \hat{\varphi}; d) \\ \text{Lin } G^d(d, d^*; \varphi)|_{\bar{\varphi}, \bar{d}} &:= G^d(\bar{d}, d^*; \bar{\varphi}) + \Delta G^d(d, d^*, \hat{d}; \varphi)\end{aligned}\quad (4.3)$$

Please note that, the operator splitting algorithm proposed in [20] is used here, hence the staggered solution procedure will be conducted, see Figure 4.1 for the solution diagram. Therefore, off diagonal tangential terms are not used. Since the variable  $d$  in the functional  $\text{Lin } G^\varphi$  and the variable  $\varphi$  in the functional  $\text{Lin } G^d$  are taken from the previous time step  $(d_n, \varphi_n)$ ,  $\Delta G^d$  and  $\Delta G^\varphi$  are not functions of  $\hat{\varphi}$  and  $\hat{d}$ , respectively. The incremental functionals are then expressed as

$$\begin{aligned}\Delta G^\varphi &= \Delta G_{\text{int}}^\varphi - \Delta G_{\text{ext}}^\varphi \\ \Delta G^d &= \Delta G_{\text{int}}^d - \Delta G_{\text{ext}}^d\end{aligned}\quad (4.4)$$

Where the internal Galerkin functional for the mechanical problem is defined as

$$\Delta G_{\text{int}}^\varphi(\varphi, \varphi^*, \hat{\varphi}; d) = \int_{\mathcal{B}} \Delta(\nabla_x \varphi^*) : \boldsymbol{\tau} dV + \int_{\mathcal{B}} \nabla_x \varphi^* : \Delta \boldsymbol{\tau} dV \quad (4.5)$$

with the incremental term  $\Delta \nabla_x \varphi^*$  being derived as,

$$\begin{aligned}\Delta(\nabla_x \hat{\varphi}) &= \Delta(\nabla_X \hat{\varphi} \mathbf{F}^{-1}) = \nabla_X \hat{\varphi} \Delta \mathbf{F}^{-1} \\ &= -\nabla_X \varphi^* (\mathbf{F}^{-1} \Delta(\mathbf{F}) \mathbf{F}^{-1}) \\ &= -\nabla_x \varphi^* \nabla_x \hat{\varphi},\end{aligned}\quad (4.6)$$

and the incremental stress  $\Delta \boldsymbol{\tau}$  is obtained as,

$$\begin{aligned}\Delta \boldsymbol{\tau} &= \boldsymbol{\mathcal{L}}_{\hat{\varphi}} \boldsymbol{\tau} + \nabla_x \hat{\varphi} \boldsymbol{\tau} + \boldsymbol{\tau} (\nabla_x \hat{\varphi})^T \\ &= \mathbb{C} : \nabla_x \hat{\varphi} + \nabla_x \hat{\varphi} \boldsymbol{\tau} + \boldsymbol{\tau} (\nabla_x \hat{\varphi})^T\end{aligned}\quad (4.7)$$

Moreover, the incremental internal Galerkin functional for the damage problem is derived as

$$\begin{aligned}\Delta G_{\text{int}}^d(d, d^*, \hat{d}; \varphi) &= \int_{\mathcal{B}} \nabla_x d^* \frac{\partial \hat{q}}{\partial \nabla_x d} \nabla_x \hat{d} dV + \int_{\mathcal{B}} d^* \frac{\partial \beta \Delta}{\partial d} dV \\ &\quad + \int_{\mathcal{B}} d^* \frac{\partial f \Delta}{\partial d} dV.\end{aligned}\quad (4.8)$$

Combining the results obtained in Equations (4.4)-(4.8), we end up with

$$\begin{aligned}\Delta G^\varphi(\varphi, \varphi^*, \hat{\varphi}; d) &= \int_{\mathcal{B}} \nabla_x \varphi^* : \mathbb{C} : \nabla_x \hat{\varphi} dV + \int_{\mathcal{B}} \nabla_x \varphi^* : \nabla_x \hat{\varphi} \boldsymbol{\tau} dV, \\ \Delta G^d(d, d^*, \hat{d}; \varphi) &= \int_{\mathcal{B}} \nabla_x d^* \cdot \frac{\partial \hat{q}}{\partial \nabla_x d} \nabla_x \hat{d} dV + \int_{\mathcal{B}} d^* \left( \frac{\partial \beta}{\partial d} + \frac{\partial f}{\partial d} \right) \hat{d} dV\end{aligned}\quad (4.9)$$

Note that externally applied loads are assumed to be deformation-independent, thus  $\Delta G_{\text{ext}}^{\varphi} = 0$ . In order to describe and solve the given continuous equations (4.3), whole body is discretized into  $nel$  subdomains  $\mathcal{B} \approx \mathcal{B}^h = \cup_{e=1}^{nel} \mathcal{B}_e^h$  the so-called finite elements. Consider discretization over the element domain  $\mathcal{B}_e$

$$\begin{aligned}
\varphi_e^h &= \sum_{i=1}^n N^i \mathbf{d}_i^e & d_e^h &= \sum_{i=1}^n N^i \phi_i^e \\
\varphi_e^{*h} &= \sum_{i=1}^n N^i \mathbf{d}_i^{*e} & d_e^{*h} &= \sum_{i=1}^n N^i \phi_i^{*e} \\
\varphi_e^{\Delta h} &= \sum_{i=1}^n N^i \mathbf{d}_i^{\Delta e} & d_e^{\Delta h} &= \sum_{i=1}^n N^i \phi_i^{\Delta e} \\
\nabla_x \varphi_e^h &= \sum_{i=1}^n \mathbf{d}_i^e \otimes \nabla_x N^i & \nabla_x d_e^h &= \sum_{i=1}^n \phi_i^e \otimes \nabla_x N^i \\
\nabla_x \varphi_e^{*h} &= \sum_{i=1}^n \mathbf{d}_i^{*e} \otimes \nabla_x N^i & \nabla_x d_e^{*h} &= \sum_{i=1}^n \phi_i^{*e} \otimes \nabla_x N^i \\
\nabla_x \varphi_e^{\Delta h} &= \sum_{i=1}^n \mathbf{d}_i^{\Delta e} \otimes \nabla_x N^i & \nabla_x d_e^{\Delta h} &= \sum_{i=1}^n \phi_i^{\Delta e} \otimes \nabla_x N^i
\end{aligned} \tag{4.10}$$

where  $\mathbf{d}$  and  $\phi$  are nodal solutions. By using discrete expressions (4.10) with combination of equations (4.3), we end up with following residual expressions,

$$\begin{aligned}
\mathbf{R}_I^{\varphi} &= \mathbf{A}_{e=1}^{nel} \left\{ \int_{\mathcal{B}_e^h} \nabla_x N^i \cdot \boldsymbol{\tau} dV - \int_{\mathcal{B}_e^h} N^i \cdot \mathbf{B} dV - \int_{\partial \mathcal{B}_e^e} N^i \cdot \mathbf{T} dA \right\} \\
R_J^d &= \mathbf{A}_{e=1}^{nel} \left\{ \int_{\mathcal{B}_e^h} \nabla_x N^j \cdot \hat{\mathbf{q}} dV + \int_{\mathcal{B}_e^h} N^j \beta dV + \int_{\mathcal{B}_e^h} N^j f dV \right\}.
\end{aligned} \tag{4.11}$$

Expressions that contain mixed derivatives  $\mathbf{K}^{\varphi d}$  and  $\mathbf{K}^{d\varphi}$  are set to zero, due to the proposed staggered solution scheme.

$$\begin{aligned}
\mathbf{K}_{IJ-mat}^{\varphi\varphi} &= \mathbf{A}_{e=1}^{nel} \left\{ \int_{\mathcal{B}_e^h} \nabla_x N^i \cdot \mathbb{C} \cdot \nabla_x N^j dV \right\} \\
\mathbf{K}_{IJ-geo}^{\varphi\varphi} &= \mathbf{A}_{e=1}^{nel} \left\{ \int_{\mathcal{B}_e^h} \nabla_x N^i \cdot (\nabla_x N^j \boldsymbol{\tau}) dV \right\} \\
\mathbf{K}_{IJ}^{dd} &= \mathbf{A}_{e=1}^{nel} \left\{ \int_{\mathcal{B}_e^h} \nabla_x N^i \frac{\partial \hat{\mathbf{q}}}{\partial \nabla_x d} \nabla_x N^j dV + \int_{\mathcal{B}_e^h} N^i \left( \frac{\partial \beta}{\partial d} + \frac{\partial f}{\partial d} \right) N^j dV \right\}
\end{aligned} \tag{4.12}$$

where  $\mathbf{A}$ , the assembly operator, assembles the contribution of each nodal value  $i, j = 1, 2, \dots, n_{en}$  to provide global nodal values  $I, J = 1, 2, 3, \dots, n_{nd}$ . The final

solution scheme of the staggered algorithm results in

$$\begin{aligned} \mathbf{d} &= \bar{\mathbf{d}} - \bar{\mathbf{K}}^{-\varphi\varphi^{-1}} \cdot \bar{\mathbf{R}}^\varphi \\ \phi &= \bar{\phi} - \bar{\mathbf{K}}^{dd^{-1}} \bar{\mathbf{R}}^d \end{aligned} \tag{4.13}$$

In a general staggered solution scheme, Equations (4.13) are solved separately and successively by using the values of the other variable taken from the previous time step, Figure 4.1. Since Equations (4.13) are solved separately, terms that contain mixed derivatives in the stiffness matrix are not needed, and are thus set to zero.

$$\mathbf{K}^{\varphi d} = \mathbf{0}, \quad \mathbf{K}^{d\varphi} = \mathbf{0} \tag{4.14}$$

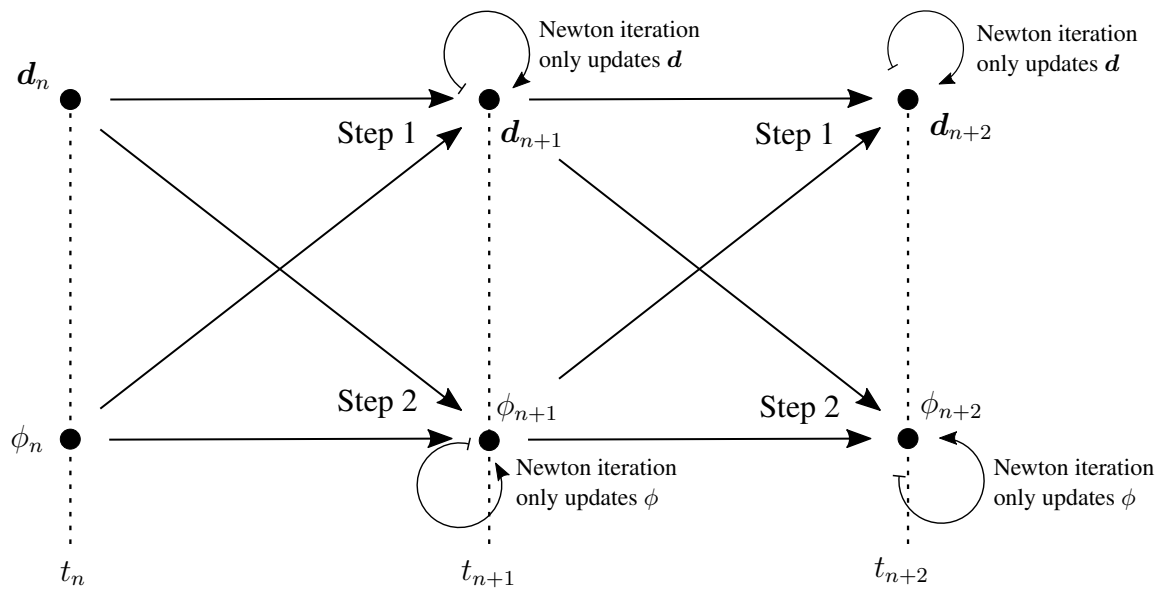


Figure 4.1: Staggered solution scheme of the coupled problem.

## CHAPTER 5

### SPECIFICATION OF CONSTITUTIVE MODELS

The chapter outlines two distinct approaches of Miehe and Schänzel [20] and Talamini, Mao and Anand [25] to rupture of rubbery polymers, and extends the latter approach to the Non-affine Microsphere framework. Therefore, the whole chapter is divided into three parts.

1. Non-affine Microsphere model of hyperelasticity [35].
2. Rubber fracture model I: Neo-Hookean-type hyperelasticity coupled with the Phase-field model [20].
3. Rubber fracture model II: Microsphere extension of the bond-stretch model coupled with the Phase-field model [25].

In Section 5.1, the so called the *non-affine microsphere* model will be presented [35]. Single chain mechanics and homogenization through the microsphere will be discussed. In Section 5.2, the Neo-Hookean-type hyperelasticity model coupled with the Phase-field model for finite elasticity will be explained. In Section 5.3, the Microsphere extension of the bond-stretch model coupled with the Phase-field model will be explained and necessary expressions for the coupled phase-field problem will be derived.

In the geometrically nonlinear setting, as introduced in Chapter 2, the response of a solid body is described by the nonlinear deformation map.

$$\varphi := \begin{cases} \mathcal{B} \times T \rightarrow \mathcal{S} \\ \mathbf{X} \mapsto \mathbf{x} = \varphi(\mathbf{X}, t) \end{cases} \quad (5.1)$$

which maps the material points  $\mathbf{X}$  in the material body  $\mathcal{B}$  on to the spatial points  $\mathbf{x}$  in the spatial body  $\mathcal{S}$ . The free energy of a solid is assumed to be a function of the deformation gradient  $\mathbf{F} = \nabla_{\mathbf{X}}\varphi$ .

$$\Psi = \hat{\Psi}(\mathbf{g}; \mathbf{F}) \quad (5.2)$$

where  $\mathbf{g}$  is the spatial metric tensor defined in (2.11). The stresses and moduli expressions are derived as

$$\boldsymbol{\tau} = 2\partial_{\mathbf{g}}\Psi(\mathbf{g}; \mathbf{F}) \quad \mathbb{C} = 4\partial_{\mathbf{g}\mathbf{g}}^2\Psi(\mathbf{g}; \mathbf{F}) \quad (5.3)$$

Most rubber-like materials exhibit nearly incompressible behavior. For this purpose, we decouple the energy function into volumetric and isochoric parts.

$$\Psi(\mathbf{g}; \mathbf{F}) = U(J) + \bar{\Psi}(\mathbf{g}; \bar{\mathbf{F}}) \quad (5.4)$$

Therefore, the stress expression also splits into volumetric and deviatoric parts, accordingly.

$$\boldsymbol{\tau} = s\mathbf{1} + \bar{\boldsymbol{\tau}} : \mathbb{P} \quad (5.5)$$

The corresponding moduli expression is obtained as

$$\begin{aligned} \mathbb{C} = (s + k)\mathbf{1} \otimes \mathbf{1} - 2s\mathbb{I} + \mathbb{P}^T : \left[ \bar{\mathbb{C}} + \frac{2}{3}(\bar{\boldsymbol{\tau}} : \mathbf{1})\mathbb{I} \right] : \mathbb{P} \\ - \frac{2}{3}(\mathbb{P}^T : \bar{\boldsymbol{\tau}} \otimes \mathbf{1} + \mathbf{1} \otimes \bar{\boldsymbol{\tau}} : \mathbb{P}) \end{aligned} \quad (5.6)$$

where the fourth-order identity tensor and the deviatoric projection tensor are defined as

$$\begin{aligned} \mathbb{I}_{ijkl} &= \frac{1}{2}(\delta_{ik}\delta_{jl} + \delta_{il}\delta_{jk}) \\ \mathbb{P}_{ijkl} &= \mathbb{I}_{ijkl} - \frac{1}{3}\delta_{ij}\delta_{kl}. \end{aligned} \quad (5.7)$$

The volumetric terms that appear in Equations (5.5) and (5.6) are defined as

$$s := JU'(J) \quad k := J^2U''(J) \quad (5.8)$$

The isochoric terms that depend on the isochoric part of the deformation gradient are defined as

$$\bar{\boldsymbol{\tau}} := 2\partial_{\mathbf{g}}\bar{\Psi}(\mathbf{g}; \bar{\mathbf{F}}) \quad \bar{\mathbb{C}} := 4\partial_{\mathbf{g}\mathbf{g}}^2\bar{\Psi}(\mathbf{g}; \bar{\mathbf{F}}) \quad (5.9)$$

More detailed derivation of the volumetric-isochoric decoupling formulation can be found in [41, 39].

## 5.1 Non-affine Microsphere Model of Hyperelasticity

The idea behind most of the elasticity models for natural rubber is based on the single chain mechanics [43, 44, 45, 46]. The micromechanical response of polymer molecules is based on their entropic change. In statistical mechanics, the entropy of a body is calculated through the *Boltzmann Equation*.

$$\eta = k \ln p \quad (5.10)$$

where  $k$  is the Boltzmann constant and  $p$  is the probability density function of the vector which is located between the two ends of the chain molecule, often referred to as the *end-to-end* vector  $r$ .

### 5.1.1 Contribution of the Free Chain

In order to truly express the force-extension relation for the high extension values, the non-Gaussian model introduced in [47] is used. The distribution function of the end-to-end distance  $r$  for the proposed model given as

$$p_f(r) = p_0 \exp \left[ -N \left( \frac{r}{Nl} \mathcal{L}^{-1} \left( \frac{r}{Nl} \right) + \ln \frac{\mathcal{L}^{-1} \left( \frac{r}{Nl} \right)}{\sinh \mathcal{L}^{-1} \left( \frac{r}{Nl} \right)} \right) \right] \quad (5.11)$$

where subscript  $f$  denotes the *free chain*. The considered polymer chain is composed of  $N$  Kuhn segments each with length  $l$  as depicted in Figure 5.1. Hence, the full chain contour length is  $L = Nl$ . For an unstrained chain molecule, the mean end-to-end distance assumed to be  $r_0 = \sqrt{Nl}$  for all molecules in network. Note that,  $r_0$  is not the most probable location of the end of the chain, it is the most probable distance between the end points of chain [33] p.52. Since  $r_0$  is the rest end-to-end distance and  $r$  is the current end-to-end distance, stretch in a single chain is defined as  $\lambda = r/r_0$ . To ease the formulation, the relative stretch  $\lambda_r$  is defined as a ratio of the end-to-end distance  $r$  to the fully extended length  $L$ .

$$\lambda := \frac{r}{r_0} = \frac{r}{\sqrt{Nl}} \quad \lambda_r := \frac{r}{L} = \frac{r}{Nl} = \frac{\lambda}{\sqrt{N}} \quad (5.12)$$

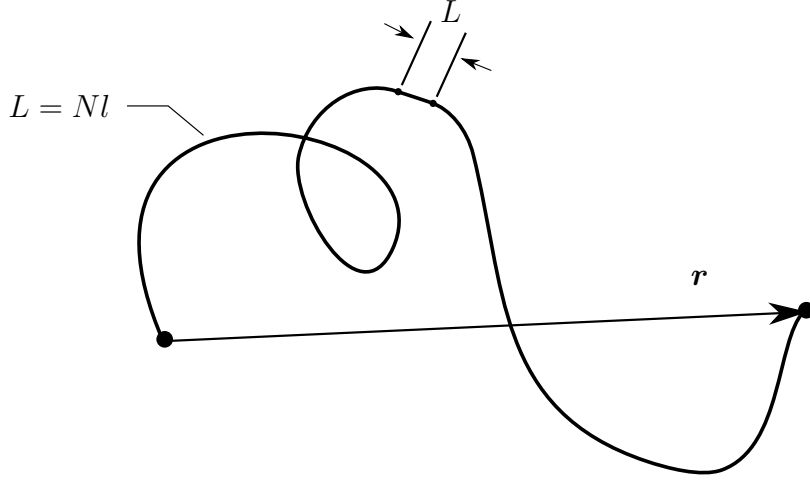


Figure 5.1: Idealized single chain composed of  $N$  Kuhn segments each with length  $l$ .

with  $\lambda \in [0, \sqrt{N})$  and  $\lambda_r \in [0, 1)$ . By definitions (5.12) at hand, Equation (5.11) can be rearranged as,

$$p_f(\lambda_r) = p_0 \exp \left[ -N \left( \lambda_r \beta + \ln \frac{\beta}{\sinh \beta} \right) \right] \quad \text{with} \quad \beta := \mathcal{L}^{-1}(\lambda_r). \quad (5.13)$$

Substituting this probability density function into the Boltzmann equation (5.10), we end up with the free energy of an unconstrained single chain.

$$\psi_f(\lambda) = Nk\theta \left( \lambda_r \beta + \ln \frac{\beta}{\sinh \beta} \right) + \psi_{f0} \quad (5.14)$$

where  $\psi_{f0}$  is the normalization constant.

### 5.1.2 Contribution of the Tube-like Constraint

In the classical treatment of the chain molecules, long polymer chains idealized by freely rotating chains [48]. This idealized behavior does not truly express the constraint motion of a single chain in the polymer network. This constraint is mostly caused by cross-linking and entanglements. In order to account for these constraints, a polymer chain is assumed to be confined in a tube [49] p.205. This tube acts as an obstacle against the free movement of a chain, like natural obstacles. The probability function of the tube constraint given as

$$p_c(\nu) = p_0 \exp \left\{ -\alpha \left( \frac{r_0}{d_0} \right)^2 \nu \right\} \quad (5.15)$$

where  $\nu$  is defined as the area contraction of the tube

$$\nu := \left( \frac{d_0}{d} \right)^2 \quad (5.16)$$

where  $d_0$  is the initial diameter of the tube and subscript  $c$  stands for *constraint*. Substituting the probability function of the tube constraint into the Boltzmann equation (5.10) we obtain the tube free energy.

$$\psi_c(\nu) = \alpha k \theta N \left( \frac{l}{d_0} \nu \right) + \psi_{c0} \quad (5.17)$$

where  $\psi_{c0}$  is a normalization constant.

The probability of the end-to-end distance and the tube constraints are assumed to be independent of each other. The total probability function can then be expressed as

$$p(\lambda, \nu) = p_f(\lambda) p_c(\nu) \quad (5.18)$$

Therefore, the free energy splits additively,

$$\psi(\lambda, \nu) = \psi_f(\lambda) + \psi_c(\nu) \quad (5.19)$$

with the corresponding free energies,

$$\begin{aligned} \psi_f(\lambda) &= N k \theta \left( \lambda_r \beta + \ln \frac{\beta}{\sinh \beta} \right) + \psi_{f0} \\ \psi_c(\nu) &= \alpha N k \theta \left( \frac{l}{d_0} \right)^2 \nu + \psi_{c0} \end{aligned} \quad (5.20)$$

### 5.1.3 Micro-Macro Bridging of State Variables

The main concept of network theories is to connect the behavior of the single chain to the behavior of the whole network. This connection is made through the averaging of the micro stretches over a unit sphere in order to relate them to macro stretches, i.e.  $\bar{\lambda}, \bar{\nu}$ . The additive split of the microscopic free energy leads to an additive split in the macroscopic free energy.

$$\bar{\Psi}(\mathbf{g}; \bar{\mathbf{F}}) = \Psi_f(\mathbf{g}; \bar{\mathbf{F}}) + \Psi_c(\mathbf{g}; \bar{\mathbf{F}}) \quad (5.21)$$

$\Psi_f$  is the energy contribution from the free movement of chains constituting the network, whereas  $\Psi_c$  is the energy contribution from the constrained movement of the

chains. As a consequence of (5.21), the stress response and moduli expression also split into two parts.

$$\bar{\boldsymbol{\tau}} = \boldsymbol{\tau}_f + \boldsymbol{\tau}_c \quad \text{and} \quad \bar{\mathbb{C}} = \mathbb{C}_f + \mathbb{C}_c \quad (5.22)$$

with corresponding derivatives,

$$\begin{aligned} \boldsymbol{\tau}_f &= 2\partial_{\mathbf{g}}\Psi_f(\mathbf{g}; \bar{\mathbf{F}}) & \text{and} & & \boldsymbol{\tau}_c &= 2\partial_{\mathbf{g}}\Psi_c(\mathbf{g}; \bar{\mathbf{F}}) \\ \mathbb{C}_f &= 4\partial_{\mathbf{g}\mathbf{g}}^2\Psi_f(\mathbf{g}; \bar{\mathbf{F}}) & & & \mathbb{C}_c &= 4\partial_{\mathbf{g}\mathbf{g}}^2\Psi_c(\mathbf{g}; \bar{\mathbf{F}}) \end{aligned} \quad (5.23)$$

### 5.1.3.1 Free Chain Contribution

Despite the fact that models with affine deformation treatment [50], [34] perform well in some cases, in a real polymeric network, chains deform differently. Although sufficiently large bodies behave similarly under the same loadings, in micro-scale, they distort differently due to the distinctive alignment of the chains in the polymeric network. In other words, under a homogeneous deformation, not all the sufficiently small material points are deformed homogeneously. To this end, micro-stretches are allowed to fluctuate over a unit microsphere, that is

$$\lambda = \bar{\lambda}f(\theta, \phi) \quad (5.24)$$

with  $\theta$  and  $\phi$  being the spherical coordinates. For affine deformation, the stretch fluctuation field would become  $f = 1$ . The non-affine micro-stretches constrained by

$$\langle \lambda \rangle_p = \langle \bar{\lambda} \rangle_p \quad (5.25)$$

where  $\langle \bullet \rangle_p$  denotes the  $p$ -root averaging operation, defined by

$$\langle \bullet \rangle_p = \sqrt[p]{\langle \bullet \rangle^p} = \left\{ \frac{1}{|S|} \int_S (\bullet)^p dA \right\}^{1/p} \quad (5.26)$$

It is postulated that the micro stretches are assumed to fluctuate in a way that, these fluctuations minimize the macroscopic free energy. This constrained minimization problem is expressed as

$$\Psi_f(\mathbf{g}; \mathbf{F}) = \sup_K \inf_f \left\{ \langle n\psi_f(\bar{\lambda}f) \rangle - K(\langle \bar{\lambda}f \rangle_p - \langle \bar{\lambda} \rangle_p) \right\} \quad (5.27)$$

where the Lagrange multiplier  $K$  dictates  $\langle \lambda \rangle_p = \langle \bar{\lambda} \rangle_p$ . The minimum free energy with respect to  $f$  can be calculated by taking the derivative with respect to  $f$ .

$$n\psi'_f(\bar{\lambda}f)\bar{\lambda} - K\left(\langle \bar{\lambda}f \rangle_p^{1-p}(\bar{\lambda}f)^{p-1}\bar{\lambda}\right) = 0 \quad (5.28)$$

rearranging the latter expression, we arrive at

$$K = \frac{n\psi'_f(\bar{\lambda}f)(\theta, \phi)}{\langle \bar{\lambda}f \rangle_p^{1-p}(\bar{\lambda}f)^{p-1}}. \quad (5.29)$$

Since  $K$  is constant, only admissible solution can be derived if and only if  $\lambda = \bar{\lambda}f$  is constant. Then Equation (5.25) takes the form,

$$\lambda = \langle \bar{\lambda} \rangle_p \quad (5.30)$$

and the free energy turns into

$$\Psi_f(\mathbf{g}; \bar{\mathbf{F}}) = n\psi(\langle \bar{\lambda} \rangle_p) \quad (5.31)$$

### 5.1.3.2 Tube Contribution

A non-linear relation between the micro-tube contraction and the macro-area-stretch is assumed

$$\nu = \bar{\nu}^q. \quad (5.32)$$

Since the relation between the micro and the macro variables are non-linear, the energy contribution of the tube contraction is calculated by

$$\Psi_c(\mathbf{g}; \bar{\mathbf{F}}) = \langle n\psi_c(\bar{\nu}^q) \rangle. \quad (5.33)$$

### 5.1.4 Stress and Moduli Expressions

**Free Chain Contribution.** Let  $\mathbf{r}$  be an arbitrary orientation unit vector which emanates from the origin. The deformed position of this orientation vector is calculated as

$$\mathbf{t} = \bar{\mathbf{F}}\mathbf{r} \quad (5.34)$$

where  $\mathbf{t}$  is the deformed stretch vector. Note that,  $\mathbf{r}$  is not a single vector but an arbitrary vector which could possibly take any orientational direction over the unit sphere. The macro stretch  $\bar{\lambda}$  for an orientation vector  $\mathbf{r}$  is expressed as

$$\bar{\lambda} = \sqrt{\mathbf{t} \cdot \mathbf{t}} \quad \text{since} \quad \|\mathbf{r}\| = 1 \quad (5.35)$$

the micro stretch  $\lambda$  has already been derived as

$$\lambda = \langle \bar{\lambda} \rangle_p \quad (5.36)$$

By using the first equation of (5.23), the stress contribution of the free chain can be calculated as

$$\boldsymbol{\tau}_f = 2\partial_{\mathbf{g}}\Psi_f(\mathbf{g}; \bar{\mathbf{F}}) = 2\partial_{\mathbf{g}}(n\psi_f(\lambda)) = n\partial_{\lambda}\psi_f(\lambda) \cdot 2\partial_{\mathbf{g}}\lambda \quad (5.37)$$

where

$$\partial_{\lambda}\psi_f = \sqrt{N}k\theta\beta \quad (5.38)$$

and

$$\begin{aligned} 2\partial_{\mathbf{g}}\lambda &= 2\partial_{\mathbf{g}}\left[\frac{1}{|S|}\int_S \bar{\lambda}^p dA\right]^{1/p} = \frac{1}{p}\left[\frac{1}{|S|}\int_S \bar{\lambda}^p dA\right]^{\frac{1-p}{p}}\left[\frac{1}{|S|}\int_S \partial_{\mathbf{g}}\bar{\lambda}^p dA\right] \\ &= \frac{1}{p}\lambda^{1-p}p\left[\frac{1}{|S|}\int_S \bar{\lambda}^{p-1}\frac{1}{\bar{\lambda}}\mathbf{t} \otimes \mathbf{t} dA\right] \\ &= \lambda^{1-p}\langle \bar{\lambda}^{p-2}\mathbf{t} \otimes \mathbf{t} \rangle \end{aligned} \quad (5.39)$$

with  $2\partial_{\mathbf{g}}\bar{\lambda} = \bar{\lambda}^{-1}\mathbf{t} \otimes \mathbf{t}$ . Hence, the overall stress expression is

$$\boldsymbol{\tau}_f = \sqrt{N}k\theta\beta\lambda^{1-p}\langle \bar{\lambda}^{p-2}\mathbf{t} \otimes \mathbf{t} \rangle \quad (5.40)$$

with the corresponding tangent moduli

$$\begin{aligned} \mathbb{C}_f &= 2\partial_{\mathbf{g}}\boldsymbol{\tau}_f = n\sqrt{N}k\theta 2\partial_{\mathbf{g}}\left[\beta\lambda^{1-p}\langle \bar{\lambda}^{p-2}\mathbf{t} \otimes \mathbf{t} \rangle\right] \\ &= n\sqrt{N}k\theta\left[\beta'\frac{1}{\sqrt{N}}\lambda^{1-p}\langle \bar{\lambda}^{p-2}\mathbf{t} \otimes \mathbf{t} \rangle \otimes \left(\lambda^{1-p}\langle \bar{\lambda}^{p-2}\mathbf{t} \otimes \mathbf{t} \rangle\right) \right. \\ &\quad + (1+p)\beta\lambda^{-p}\langle \bar{\lambda}^{p-2}\mathbf{t} \otimes \mathbf{t} \rangle \otimes \left(\lambda^{1-p}\langle \bar{\lambda}^{p-2}\mathbf{t} \otimes \mathbf{t} \rangle\right) \\ &\quad \left. + \beta\lambda^{1-p}\langle [p-2]\bar{\lambda}^{p-3}\mathbf{t} \otimes \mathbf{t} \otimes \left(\frac{1}{\bar{\lambda}}\mathbf{t} \otimes \mathbf{t}\right)\rangle\right] \end{aligned} \quad (5.41)$$

To express the terms (5.40) and (5.41) in a more compact way, we introduce the second order tensor  $\mathbf{h}$  and the fourth order tensor  $\mathbb{H}$  as

$$\begin{aligned}\mathbf{h} &:= \langle \bar{\lambda}^{p-2} \mathbf{t} \otimes \mathbf{t} \rangle \\ \mathbb{H} &:= \langle (p-2) \bar{\lambda}^{p-4} \mathbf{t} \otimes \mathbf{t} \otimes \mathbf{t} \otimes \mathbf{t} \rangle.\end{aligned}\quad (5.42)$$

Using these tensors in the stress and moduli expressions, we obtain

$$\begin{aligned}\boldsymbol{\tau}_f &= \sqrt{N} \mu \beta \lambda^{1-p} \mathbf{h} \\ \mathbb{C}_f &= (\mu \beta' \lambda^{2(1-p)} + \mu \sqrt{N} \beta (1-p) \lambda^{1-2p}) \mathbf{h} \otimes \mathbf{h} + \mu \beta \sqrt{N} \lambda^{1-p} \mathbb{H}\end{aligned}\quad (5.43)$$

where  $\mu := nk\theta$  defined as the shear modulus, and  $\beta, \beta'$  are calculated by the Padé's approximation

$$\beta = \mathcal{L}^{-1}(\lambda_r) \approx \lambda_r \frac{3 - \lambda_r^2}{1 - \lambda_r^2}, \quad \beta' = \frac{\partial \beta}{\partial \lambda_r} = \frac{\lambda_r^4 + 3}{(1 - \lambda_r^2)^2} \quad (5.44)$$

**Tube Contribution.** The deformed configuration of the normal vector  $\mathbf{r}$  is calculated as,

$$\mathbf{n} = \bar{\mathbf{F}}^{-T} \mathbf{r} \quad (5.45)$$

where  $\mathbf{n}$  is the deformed normal vector. Macro-area-stretch  $\bar{\nu}$  for normal vector  $\mathbf{r}$  is expressed as,

$$\bar{\nu} = \sqrt{\mathbf{n} \cdot \mathbf{g}^{-1} \mathbf{n}} \quad (5.46)$$

Micro-tube contraction is already introduced in (5.32). By using the stress equation (5.23), the stress contribution of the tube constraint can be calculated as

$$\begin{aligned}\boldsymbol{\tau}_c &= 2\partial_{\mathbf{g}} \Psi_c(\mathbf{g}; \mathbf{F}) = 2\partial_{\mathbf{g}} \langle n\psi_c(\nu) \rangle \\ \boldsymbol{\tau}_c &= - \left\langle nk\theta\alpha \left(\frac{l}{d_0}\right)^2 Nq\bar{\nu}^{q-2} \mathbf{n} \otimes \mathbf{n} \right\rangle\end{aligned}\quad (5.47)$$

and the corresponding moduli expression is derived as

$$\begin{aligned}\mathbb{C}_c &= 2\partial_{\mathbf{g}} \boldsymbol{\tau}_c \\ \mathbb{C}_c &= \left\langle nk\theta\alpha \left(\frac{l}{d_0}\right)^2 Nq(q-2) \bar{\nu}^{q-4} \mathbf{n} \otimes \mathbf{n} \otimes \mathbf{n} \otimes \mathbf{n} \right. \\ &\quad \left. + nk\theta\alpha \left(\frac{l}{d_0}\right)^2 Nq\bar{\nu}^{q-2} \mathbb{Q} \right\rangle\end{aligned}\quad (5.48)$$

with the fourth order tensor  $\mathbb{Q}$  defined in indicial notation

$$\mathbb{Q}_{abcd} = (g_{bd}^{-1} n_a n_c + g_{bc}^{-1} n_a n_d) + (g_{ac}^{-1} n_b n_d + g_{ad}^{-1} n_b n_c) \quad (5.49)$$

To express terms (5.47) and (5.48) in a more compact way, we introduce the second order tensor  $\mathbf{k}$  and the fourth order tensor  $\mathbb{K}$  as

$$\begin{aligned}\mathbf{k} &:= \langle q \bar{\nu}^{q-2} \mathbf{n} \otimes \mathbf{n} \rangle \\ \mathbb{K} &:= \langle q(q-2) \bar{\nu}^{q-4} \mathbf{n} \otimes \mathbf{n} \otimes \mathbf{n} \otimes \mathbf{n} \rangle\end{aligned}\tag{5.50}$$

and rearrange the stress and the moduli expression to arrive at

$$\begin{aligned}\boldsymbol{\tau}_c &= -\mu UN \mathbf{k} \\ \mathbb{C}_c &= \mu UN (\mathbb{K} + \mathbb{Q})\end{aligned}\tag{5.51}$$

where  $U := \alpha (l/d_0)^2$  is defined as a material parameter. All the material parameters are summarized in Table 5.1.

Table 5.1: Material parameters of the Micro-sphere model

Parameter	Explanation
$\mu$	Shear modulus
$N$	Number of chain segments
$p$	Non-affine stretch parameter
$U$	Tube geometry parameter
$q$	Non-affine tube parameter

### 5.1.5 Integration Over the Sphere

Since the proposed model involves an integration over the sphere, the numerical integration is proposed for the area integration over the unit sphere. The continuous integral is approximated by a discrete weighted summation, that is,

$$\langle \mathbf{r} \rangle := \frac{1}{|S|} \int_S \mathbf{r}(\theta, \phi) dA \approx \sum_m^{i=1} r_i w_i\tag{5.52}$$

In order to retain isotropy and stress-free state under zero deformation, the integration points in [51] are used.

$$\langle \mathbf{r} \rangle = \mathbf{0} \quad \text{and} \quad \langle \mathbf{r} \otimes \mathbf{r} \rangle = \frac{1}{3} \mathbf{1}\tag{5.53}$$

Orientation vectors and their associated weights are given in Table 5.2. By exploiting the symmetry, only the points in the upper portion of the sphere are considered. For

Table 5.2: Integration points with  $x$ ,  $y$  and  $z$  coordinates and the associated weights

point	$r_i^1$	$r_i^2$	$r_i^3$	$w_i/2$
1	0.0	0.0	1.0	0.0265214244093
2	0.0	1.0	0.0	0.0265214244093
3	1.0	0.0	0.0	0.0265214244093
4	0.0	0.707106781187	0.707106781187	0.0199301476312
5	0.0	-0.707106781187	0.707106781187	0.0199301476312
6	0.707106781187	0.0	0.707106781187	0.0199301476312
7	-0.707106781187	0.0	0.707106781187	0.0199301476312
8	0.707106781187	0.707106781187	0.0	0.0199301476312
9	-0.707106781187	0.707106781187	0.0	0.0199301476312
10	0.836095596749	0.387907304067	0.387907304067	0.0250712367487
11	-0.836095596749	0.387907304067	0.387907304067	0.0250712367487
12	0.836095596749	-0.387907304067	0.387907304067	0.0250712367487
13	-0.836095596749	-0.387907304067	0.387907304067	0.0250712367487
14	0.387907304067	0.836095596749	0.387907304067	0.0250712367487
15	-0.387907304067	0.836095596749	0.387907304067	0.0250712367487
16	0.387907304067	-0.836095596749	0.387907304067	0.0250712367487
17	-0.387907304067	-0.836095596749	0.387907304067	0.0250712367487
18	0.387907304067	0.387907304067	0.836095596749	0.0250712367487
19	-0.387907304067	0.387907304067	0.836095596749	0.0250712367487
20	0.387907304067	-0.387907304067	0.836095596749	0.0250712367487
21	-0.387907304067	-0.387907304067	0.836095596749	0.0250712367487

different numerical integration schemes and error analysis the reader is referred to [52]. For the numerical implementation, the whole algorithm summarized in Table 5.3.

## 5.2 Rubber Fracture Model I: Neo-Hookean-type hyperelasticity coupled with Phase-field

In this section, we discuss the recent work of Miehe and Schänzel [20], which is proposed for the phase-field method in the geometrically nonlinear setting. We will derive the constitutive equations and summarize the numerical implementation of the proposed model.

The response of the solid undergoing fracture is described by

$$\varphi := \begin{cases} \mathcal{B} \times T \rightarrow \mathcal{S} \\ \mathbf{X} \mapsto \mathbf{x} = \varphi(\mathbf{X}, t) \end{cases} \quad \text{and} \quad d := \begin{cases} \mathcal{B} \times T \rightarrow [0, 1] \\ \mathbf{X} \mapsto d(\mathbf{X}, t) \end{cases} \quad (5.54)$$

where  $\varphi$  maps the material points  $\mathbf{X}$  to their deformed positions  $\mathbf{x}$  and  $d$  dictates the local damage state of the material at point  $\mathbf{X}$ .  $d = 0$  denotes the undamaged state and  $d = 1$  corresponds to fully fractured state. The free energy of the fracturing isotropic solid is given as a function of the deformation gradient  $\mathbf{F}$  and damage  $d$

$$\Psi(\mathbf{g}; \mathbf{F}, d) = g(d) \Psi_0(\mathbf{g}; \mathbf{F}) \quad (5.55)$$

with a monotonically decreasing degradation function  $g(d)$  and the undamaged reference free energy  $\Psi_0$ . The degradation function determines the weakened response of the damaged material and should satisfy the following constraints.

$$g' \leq 0 \quad g(0) = 1 \quad g(1) = 0 \quad g'(1) = 0. \quad (5.56)$$

The simple degradation function for the given constraints is adopted [20, 25, 53] as follows.

$$g(d) = (1 - d)^2 \quad (5.57)$$

The elastic response of the proposed model is described by following undamaged free

Table 5.3: Algorithmic Box for the Microsphere model

1. Initialization of orientational vectors  $\mathbf{r}^i$  and weights  $w^i$  for  $i = 1, 21$ .

2. Calculation of the micro-stretch  $\lambda$  and the corresponding derivatives.  $\mathbf{t}^i = \mathbf{F}\mathbf{r}^i$  and  $\bar{\lambda}^i = |\mathbf{t}^i|$

$$\lambda = \left[ \sum_{i=1}^{21} (\bar{\lambda}^i)^p w^i \cdot 2 \right]^{1/p}$$

$$\mathbf{h} = \sum_{i=1}^{21} (\bar{\lambda}^i)^{p-2} \mathbf{t}^i \otimes \mathbf{t}^i w^i \cdot 2$$

$$\mathbb{H} = \sum_{i=1}^{21} (p-2) (\bar{\lambda}^i)^{p-4} \mathbf{t}^i \otimes \mathbf{t}^i \otimes \mathbf{t}^i \otimes \mathbf{t}^i w^i \cdot 2$$

3. Coefficients for the stress  $\boldsymbol{\tau}_f$  and the moduli  $\mathbb{C}_f$ .

$$\lambda_r = \frac{\lambda}{\sqrt{N}} \quad \beta = \frac{3 - \lambda_r^2}{1 - \lambda_r^2} \lambda_r \quad \beta' = \frac{\lambda_r^4 + 3}{(1 - \lambda_r^2)^2}$$

$$\boldsymbol{\tau}_f = \mu \sqrt{N} \beta \lambda^{1-p} \mathbf{h}$$

$$\mathbb{C}_f = \left[ \mu \beta' \lambda^{2(1-p)} + \mu \beta \sqrt{N} \lambda^{1-2p} \right] \mathbf{h} \otimes \mathbf{h} + \mu \beta \sqrt{N} \lambda^{1-p} \mathbb{H}$$

4. Calculation of the micro-area-stretch and the corresponding derivatives  $\mathbf{n}^i = \mathbf{F}^{-T} \mathbf{r}^i$  and  $\bar{\nu}^i = |\mathbf{n}^i|$ .

$$\mathbf{k} = \sum_{i=1}^{21} q (\bar{\nu}^i)^{q-2} \mathbf{n}^i \otimes \mathbf{n}^i w^i \cdot 2$$

$$\mathbb{K} = \sum_{i=1}^{21} q (q-2) (\bar{\nu}^i)^{q-4} \mathbf{n}^i \otimes \mathbf{n}^i \otimes \mathbf{n}^i \otimes \mathbf{n}^i w^i \cdot 2$$

$$\mathbb{Q} = \sum_{i=1}^{21} q (\bar{\nu}^i)^{q-2} \left( n_a^i n_c^i g_{bd}^{-1} + n_a^i n_d^i g_{bc}^{-1} + n_b^i n_d^i g_{ac}^{-1} + n_b^i n_c^i g_{ad}^{-1} \right) w^i \cdot 2$$

5. Coefficients of stress  $\boldsymbol{\tau}_c$  and moduli  $\mathbb{C}_c$

$$\boldsymbol{\tau}_c = -\mu U N \mathbf{k}$$

$$\mathbb{C}_c = \mu U n (\mathbb{K} + \mathbb{Q}).$$

6. Final Stress  $\boldsymbol{\tau}$  and moduli  $\mathbb{C}$

$$\boldsymbol{\tau} = \boldsymbol{\tau}_f + \boldsymbol{\tau}_c \quad \text{and} \quad \mathbb{C} = \mathbb{C}_f + \mathbb{C}_c$$

energy

$$\Psi_0(\mathbf{g}; \mathbf{F}) = \frac{\mu}{2} (\mathbf{b} : \mathbf{g} - 3) + U(J) \quad (5.58)$$

as a Neo-Hookean-type energy form with the weakly incompressible volumetric part.

$$U(J) := \frac{\mu}{\xi} (J^{-\xi} - 1) \quad \text{with} \quad \xi = \frac{2\nu}{1 - 2\nu} \quad (5.59)$$

The parameter  $\xi$  is defined as a function of the Poisson ratio. The stress expression and the corresponding fourth-order moduli expression obtained as

$$\begin{aligned} \boldsymbol{\tau} &= 2\partial_{\mathbf{g}}\Psi(\mathbf{g}; \mathbf{F}, d) = g(d) [\mu\mathbf{b} + p\mathbf{1}] \\ \mathbb{C} &= 4\partial_{\mathbf{g}\mathbf{g}}^2\Psi(\mathbf{g}; \mathbf{F}, d) = g(d) [(p + \kappa)\mathbf{1} \otimes \mathbf{1} - 2p\mathbb{I}] \end{aligned} \quad (5.60)$$

where  $p := JU'(J)$  and  $\kappa := J^2U''(J)$ . The critical fracture surface energy derived through the multiplication of the regularized crack surface by critical energy release.

$$\gamma = \frac{g_c}{2l}d^2 + \frac{g_cl}{2}|\nabla_X d|^2 \quad (5.61)$$

Hence, the energetic force  $f$  and the crack driving force  $\beta$  defined in Equation (3.20) are obtained as

$$f = \partial_d\gamma(d, \nabla_X d) = \partial_d\left\{\frac{g_c}{2l}d^2 + \frac{g_cl}{2}|\nabla_X d|^2\right\} = \frac{g_c}{l}d \quad (5.62)$$

$$\beta = \partial_d\Psi(d, \mathbf{g}; \mathbf{F}) = -2(1 - d)\Psi_0 \quad (5.63)$$

The flux-like vector  $\mathbf{Q}$  is calculated as

$$\mathbf{Q} := \partial_{\nabla_X d}\gamma = g_cl\nabla_X d \quad (5.64)$$

Since we formulate and numerically implement the model problem in the *Eulerian configuration*, the term  $\nabla_X d$  should be converted into  $\nabla_x d = \nabla_X d\mathbf{F}^{-1}$ , and turned into Eulerian object by using the Piola-Identity (3.22).

$$\mathbf{q} = \frac{1}{J}\hat{\mathbf{q}} \quad \text{with} \quad \hat{\mathbf{q}} := g_cl\nabla_x d\mathbf{F}\mathbf{F}^T \quad (5.65)$$

Substituting the equations (5.62),(5.63), and (5.65), into (3.21), we arrive at

$$J \operatorname{div} \left( \frac{1}{J}g_cl\nabla_x d\mathbf{b} \right) + 2(1 - d)\Psi_0 - \frac{g_c}{l}d = 0 \quad (5.66)$$

To account for the irreversibility of the crack propagation, the term  $\Psi_0$  in (5.63) is replaced with the non-decreasing history field  $\mathcal{H}$  introduced in [29].

$$\mathcal{H}(t) := \max_{s \in [0, t)} \Psi_0(\mathbf{F}, \mathbf{g}, s) \quad (5.67)$$

In order to stabilize the numerical treatment of the crack propagation, the rate dependent viscous resistance term  $\eta \dot{d}$  can be added. Thus, final form of the equation (5.66) becomes

$$J \operatorname{div} \left( \frac{1}{J} \hat{\mathbf{q}} \right) - \frac{g_c}{l} d + 2(1-d) \mathcal{H} - \eta \dot{d} = 0. \quad (5.68)$$

For the update of the history field, the maximum achieved reference energy of the material is used.

$$\mathcal{H} := \begin{cases} \Psi_{0n} & \text{for } \Psi_{0n} > \mathcal{H}_n \\ \mathcal{H}_n & \text{for } \Psi_{0n} < \mathcal{H}_n \end{cases} \quad (5.69)$$

and for the time integration of rate term  $\dot{d}$ , the *Backward Euler scheme* is used.

$$\dot{d} \approx \frac{d - d_n}{\Delta t} \quad (5.70)$$

The superscript “ $n$ ” denotes the quantities belonging to the previous time step  $t_n$ , and  $\Delta t = t_{n+1} - t_n$  denotes the time increment between two consecutive solution steps.

### 5.3 Rubber fracture model II: Microsphere extension of the bond-stretch model coupled with Phase-field

This section is concerned with the microsphere model [35] extension of the recently developed model by Talamini, Mao, Anand [25]. The motivation of the bond stretch model is to divide the response of polymeric network into the internal energetic contribution and the configurational entropic contribution where the former is mainly concerned with the rupture of the network, whereas the latter is concerned with the overall stiffening stress response before the failure. In the bond stretch theory, unlike the classical Langevin chain, Kuhn segments are considered as extensible. While the interaction between the molecules contribute both internal energy and configurational entropy, stretching of the chain contributes only to the configurational entropy.

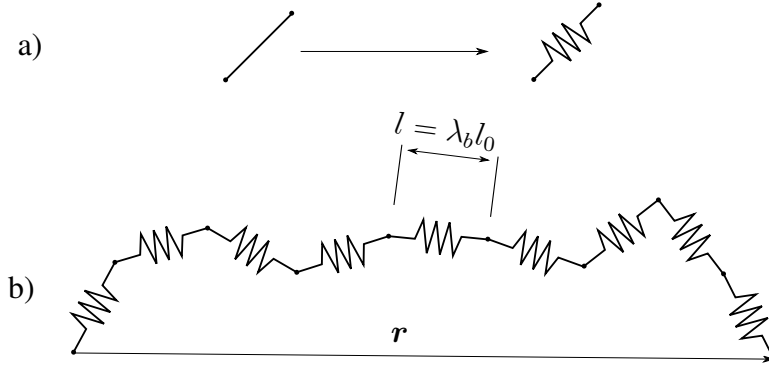


Figure 5.2: a) Kuhn segments are allowed to deform, b) Proposed single chain model.

Each segment in the Langevin chain is allowed to stretch by  $\lambda_b$ , as shown in Figure 5.2.

$$l = l_0 \lambda_b \quad (5.71)$$

where  $l$  is the current segment length and  $l_0$  is the resting segment length. The modified relative stretch  $\lambda_r$  is obtained as

$$\lambda = \frac{r}{r_0} = \frac{r}{\sqrt{N} \lambda_b l_0} \quad \lambda_r = \frac{r}{L} = \frac{r}{N \lambda_b l_0} = \frac{\lambda \lambda_b^{-1}}{\sqrt{N}} \quad (5.72)$$

Hence, the free energy contribution of the bond stretch becomes

$$\psi(\lambda, \lambda_b) = Nk\theta \left( \lambda_r \beta + \ln \frac{\beta}{\sinh \beta} \right) \quad \text{with} \quad \beta := \mathcal{L}^{-1} \left( \frac{\lambda \lambda_b^{-1}}{\sqrt{N}} \right) \quad (5.73)$$

The internal energy contribution of the interaction between the atomic bonds are given as a quadratic form.

$$\varepsilon = \frac{1}{2} N E_b (\lambda_b - 1)^2 \quad (5.74)$$

where  $E_b$  parameter can be considered as a bond stiffness. The final form of the free energy of a single chain is obtained as

$$\psi(\lambda, \lambda_b) = \frac{1}{2} N E_b (\lambda_b - 1)^2 + Nk\theta \left( \lambda_r \beta + \ln \frac{\beta}{\sinh \beta} \right) \quad (5.75)$$

For the evolution of  $\lambda_b$  the following constrained minimization problem is used.

$$\lambda_b = \arg \min_{\lambda_b^* > \lambda / \sqrt{N}} \psi(\lambda, \lambda_b^*) \quad (5.76)$$

In other words, for a given stretch state, segments realign themselves in such a way that they minimize the energy of the single-chain. At this point, since the  $\lambda_b$  reduces the relative stretch, it should not be thought to decrease the amount of chain elongation. Contrary to this, since  $\lambda_b$  increases the resting length  $r_0$  and consequently reduces the relative stretch  $\lambda_r$ , the asymptotic response of the Langevin chain for the limiting case remains always finite. Hence, the stretch  $\lambda$  of a single chain can be higher than  $\sqrt{N}$ . However, the stretch due to the segment realignment  $\lambda\lambda_b^{-1}$  should not be higher than  $\sqrt{N}$ . In other words, for any value of stretch  $\lambda$ ,  $\lambda_r$  remains less than 1.

Increasing bond stretch will increase the internal energy and consequently bring the single chain closer to the scission state. Therefore, the free energy of the single fracturing chain is given as

$$\psi(\lambda, \lambda_b, d) = g(d) \left[ \frac{1}{2} N E_b (\lambda_b - 1)^2 \right] + N k \theta \left( \lambda_r \beta + \ln \frac{\beta}{\sinh \beta} \right) \quad (5.77)$$

where the degradation function  $g(d)$  has the same properties as defined in Equation (5.56). Although the degradation function does not reduce the contribution of the configurational entropic part, an increasing resting end-to-end distance  $r_0$  decreases the relative stretch and reduces the configurational entropy contribution.

For the micro-macro bridging, microsphere model is used.

$$\lambda = \langle \bar{\lambda} \rangle_p \quad (5.78)$$

For  $p = 2$ , the microsphere model becomes exactly same as the model of [25] where the 8-chain model is employed. For the bond stretch  $\lambda_b$  and damage  $d$ , every segment and chain in the network is assumed to be stretched and damaged identically.

The isochoric part of the deformation gradient contributes to the configurational entropic part through the (5.78) and the volumetric part of the deformation gradient contributes the internal energetic part of the free energy. Therefore, constitutive equation for the energetic part given as

$$\varepsilon_0(\lambda_b, J) = \frac{1}{2} N n E_b (\lambda_b - 1)^2 + \frac{1}{8} K (J - J^{-1})^2 \quad (5.79)$$

where  $n$  is the number of chains in a unit volume and  $K$  is the bulk modulus. Hence,

overall free energy becomes

$$\Psi(\mathbf{g}; \mathbf{F}, d) = g(d) \left[ \frac{1}{2} \bar{E}_b (\lambda_b - 1)^2 + \frac{1}{8} K (J - J^{-1})^2 \right] + \mu N \left( \lambda_r \beta \ln \frac{\beta}{\sinh \beta} \right) \quad (5.80)$$

where the shear modulus  $\mu = k\theta n$  and the bond stiffness  $\bar{E}_b = E_b n N$  are material parameters. The energy minimization problem solved for finding  $\lambda_b$  then becomes

$$\frac{\partial \Psi}{\partial \lambda_b} = 0 \quad \Rightarrow \quad g(d) \bar{E}_b (\lambda_b - 1) \lambda_b - \mu \lambda_r \beta = 0 \quad (5.81)$$

For the damage evolution, the following equation is considered.

$$J \operatorname{div} \frac{1}{J} \hat{\mathbf{q}} - \varepsilon^f d + 2(1-d) \mathcal{H} - \eta \dot{d} = 0 \quad (5.82)$$

where  $\hat{\mathbf{q}} := \varepsilon^f l^2 \nabla_x d \mathbf{F} \mathbf{F}^T$  and the history variable  $\mathcal{H}$  is defined through the non-decreasing threshold function.

$$\mathcal{H}(t) := \max_{s \in [0, t]} \langle \varepsilon^0(\lambda_b(s), J(s)) - \varepsilon^f / 2 \rangle \quad \text{with} \quad \langle x \rangle = \begin{cases} 0, & x < 0 \\ x, & x > 0 \end{cases} \quad (5.83)$$

### 5.3.1 Derivation of Stress and Moduli expressions

Having the free energy defined, we can continue with the calculation of the isochoric stresses and moduli. The micro-macro transition for the stretch is the same as Equation (5.30). The isochoric stresses become, then

$$\bar{\boldsymbol{\tau}} = \tau_f \mathbf{h} \quad \text{with} \quad \tau_f = \mu \sqrt{N} \frac{1}{\lambda_b} \beta \lambda^{1-p} \quad (5.84)$$

where the inverse Langevin function approximated by the Padé approximation

$$\beta := \mathcal{L}^{-1}(\lambda_r) \approx \frac{3 - \lambda_r^2}{1 - \lambda_r^2} \lambda_r \quad \text{with} \quad \lambda_r := \frac{\lambda \lambda_b^{-1}}{\sqrt{N}} \quad (5.85)$$

The corresponding isochoric moduli are expressed in the following form

$$\bar{\mathbb{C}} = c_f \mathbf{h} \otimes \mathbf{h} + \tau_f \mathbb{H} \quad (5.86)$$

with the coefficient

$$c_f = \mu \beta' \frac{1}{\lambda_b^2} \lambda^{2(1-p)} + \mu \beta \sqrt{N} (1-p) \frac{1}{\lambda_b} \lambda^{1-2p} - \left[ \mu \beta' \frac{1}{\lambda_b^3} \lambda^{(3-2p)} + \mu \sqrt{N} \beta \frac{1}{\lambda_b^2} \lambda^{2(1-p)} \right] \frac{\partial \lambda_b}{\partial \lambda} \quad (5.87)$$

The required derivative,  $\frac{\partial \lambda_b}{\partial \lambda}$  will be calculated by using the persistency condition in the algorithmic update of the internal variable  $\lambda_b$ . For the volumetric part, the derivatives of the volumetric free energy in Equation (5.79) are obtained as

$$s = \frac{J^4 - 1}{4J^2} \quad k = \frac{3 + J^4}{4J^2} \quad (5.88)$$

The total stresses and tangent moduli are obtained by substituting the isochoric and volumetric terms in Equations (5.84),(5.86) and (5.88) into Equations (5.6) and (5.5).

The material parameters of the model are summarized in Table 5.4.

Table 5.4: Material parameters of the Bond-stretch model

Parameter	Explanation
$\mu$	Shear modulus
$K$	Bulk modulus
$N$	Number of chain segments
$\bar{E}_b$	Bond stiffness
$\varepsilon^f$	Threshold critical energy
$l$	Length scale parameter
$\eta$	Viscous regularization parameter
$p$	Non-affine stretch parameter

### 5.3.2 Algorithmic update of bond stretch

Update of the bond stretch is governed by the energy minimization problem (5.76). Once the micro-stretch is obtained, the bond stretch is updated by solving Equation (5.81) implicitly. For the numerical implementation, the iterative solution scheme is summarized in Table 5.5.

Table 5.5: Iterative Newton scheme for the update of  $\lambda_b$

1. Get database from history  $\lambda_b = \lambda_b^n$  and stretch  $\lambda$  using step 2 in Table 5.3.

2. Newton iteration scheme for  $\lambda_b$

a. Initialize expressions for residual and tangent.

$$\lambda_r = \frac{\lambda \lambda_b^{-1}}{\sqrt{N}} \quad \beta = \frac{3 - \lambda_r^2}{1 - \lambda_r^2} \lambda_r \quad \beta' = \frac{\lambda_r^4 + 3}{(1 - \lambda_r^2)^2}$$

b. Calculate residual and tangent, update  $\lambda_b$

$$r = g(d) \frac{\bar{E}_b}{\mu \sqrt{N}} (\lambda_b - 1) \lambda_b - \lambda_r \beta$$

$$r' = g(d) \frac{\bar{E}_b}{\mu \sqrt{N}} (2\lambda_b - 1) + (\beta + \lambda_r \beta') \frac{\lambda_r}{\lambda_b}$$

$$\lambda_b \leftarrow \lambda_b - \frac{r}{r'}$$

c. Check whether problem is converged.

IF ( $r < tol$ ) update history and calculate required derivative in Equation 5.87

$$\frac{\partial \lambda_b}{\partial \lambda} = (\beta + \lambda_r \beta') \frac{\lambda_r}{\lambda} \frac{1}{r'}$$

ELSE IF ( $r > tol$ ) GO TO Step a.

## CHAPTER 6

### NUMERICAL RESULTS

This chapter demonstrates the modeling capability of the proposed models. First, we investigate the effect of mesh density in a penny shape pre-cracked rectangular test specimen. Second, as a benchmark problem, we examine double-notched specimens with different notch lengths given in the experimental study [1]. All numerical analysis are conducted using the Finite Element Analysis Program (FEAP) [54].

For **Rubber Fracture Model I** introduced in Section 5, we investigate the effect of mesh density on a benchmark problem given in [20]. The specimen is 2 mm in width, 0.4 mm in height, and has a 0.2 mm notch in the center as shown in Figure 6.1. Three different element sizes are considered in the crack path. By exploiting the symmetry of the geometry of the specimen and boundary conditions, we only discretize the quarter of the test specimen. For the analysis, 13500 elements with  $h^e = 5 \times 10^{-4}$  mm element size, 10000 elements with  $h^e = 1 \times 10^{-3}$  mm element size, 4000 elements with  $h^e = 2 \times 10^{-3}$  mm element size are used in the crack path. The mesh with  $h^e = 0.002$  mm used in simulations is shown in Figure 6.1. The stress analysis is conducted with monotonic displacement-driven boundary conditions with constant displacement increment  $\Delta u = 1 \times 10^{-5}$ . Simulations are performed in plane-strain condition. The shear modulus, the Poisson's ratio, the critical fracture energy, and viscosity parameters are set to  $\mu = 5$  N/mm<sup>2</sup>,  $\nu = 0.45$ ,  $g_c = 2.4$  N/mm, and  $\eta = 1 \times 10^{-3}$ , respectively. The length scale parameter  $l$  is taken constant in all analysis and set to  $l = 0.01$  mm. The load-displacement curves for different element sizes are compared in Figure 6.2. Results converge to the solution of the smallest element sized mesh. Figure 6.4 shows the deformed geometry at Points 1 through 9 on the load-displacement curve in Figure 6.3. Principle stresses for the fracturing

specimen are given in Figure 6.5.

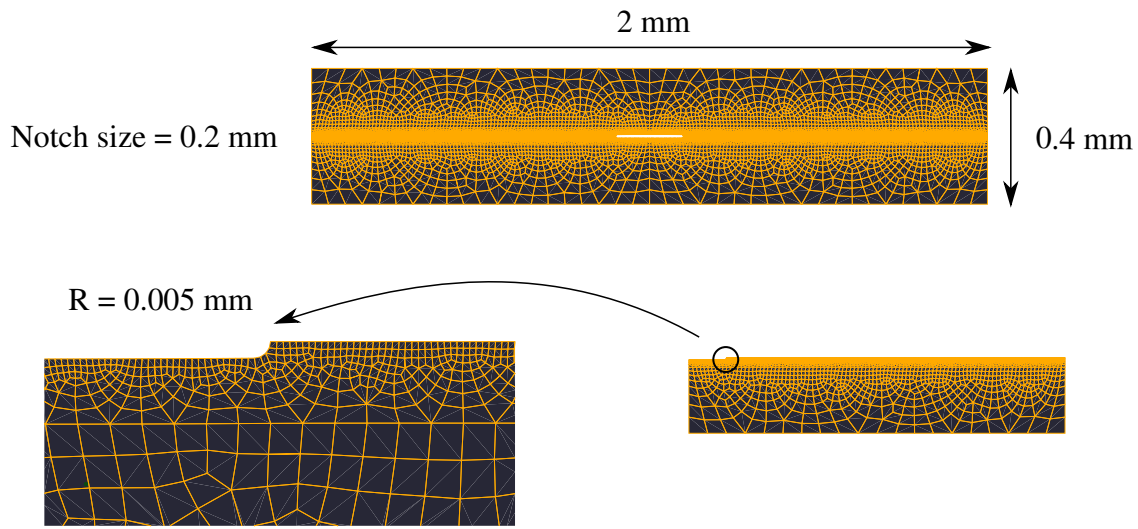


Figure 6.1: Mesh for penny shaped precracked test specimen and crack region with effective element size  $h^e = 0.002$  mm.

For **Rubber Fracture Models I and II**, we tried to reproduce the results given in [20] and [25] by using the experimental setup in [1]. The specimen is 80 mm in width, 200 mm in height and 3 mm in depth. We consider specimens with different notch lengths  $a = (16, 20, 24)$  mm with a fixed notch radius  $R = 1$  mm, see Figure 6.6 . Since the specimen is very thin, simulations are performed in plane stress condition, which is proposed in [55] and is explained in detail in [56]. In simulations, displacement of the bottom edge of the specimen kept fixed while the top edge of the specimen is subjected to monotonically increasing displacement. Displacement increments are decreased as soon as the damage has initiated due to the sudden crack propagation. By exploiting the symmetry, we discretize only the quarter of the test specimen. For the analysis, the element size of 0.05 mm is used in the crack path. For 16 mm notch size 13000 elements, for 20 mm notch size 11000 elements, for 24 mm notch size 9000 elements are used in quartile. The mesh used for simulations of the specimen with 20 mm notch size is shown in Figure 6.6. The corresponding mesh in Figure 6.6 is generated using ABAQUS/CAE [57].

The load-displacement curves for the Rubber Fracture Model I and Rubber Fracture Model II with different notch lengths are compared in Figures 6.7 and 6.8, respec-

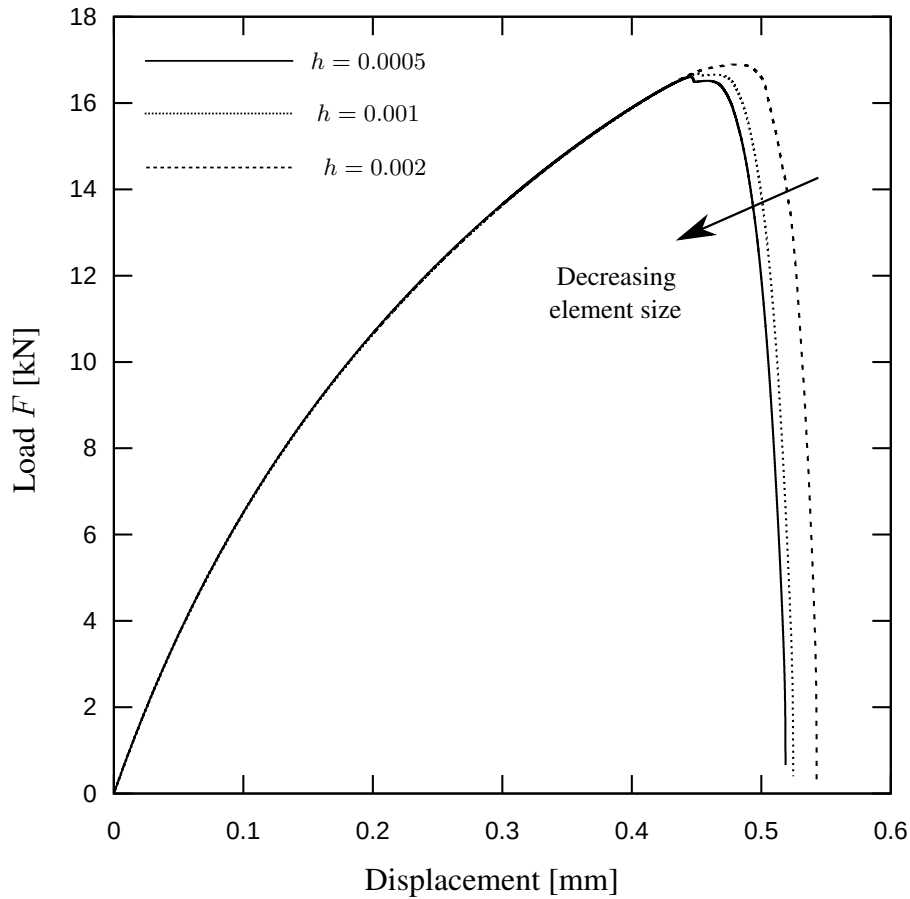


Figure 6.2: Load-displacement curves of penny shape precracked test specimens for Rubber Fracture Model I with different element sizes.

tively. In Figure 6.7a, numerical results are compared with the experimental data for the Rubber Fracture Model I. The simulations were performed in plane-strain condition. For  $a = 24$  mm and  $a = 20$  mm, the specimens could not be stretched until a fully fractured state. This could be explained with extreme element deformations. The elements around the crack deform excessively due to the non-linear geometric setting of the problem. This problem can be solved through utilizing a well structured mesh. There are some discontinuities before the sharp decrease in load values. These could be explained by the sudden change in the time increment value. An adaptive time stepping method could overcome this problem. In Figure 6.7b, numerical results are compared with the experimental data for the Rubber Fracture Model I. Simulations were performed in plane-stress condition.

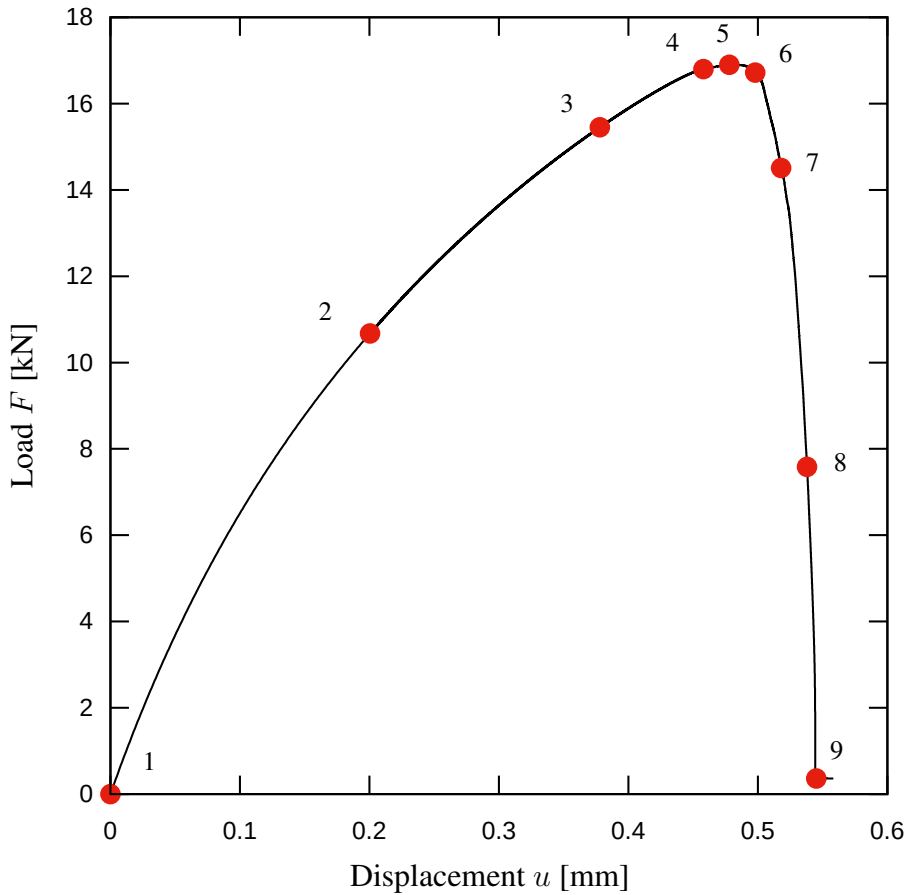


Figure 6.3: Penny shaped tension test for Rubber Fracture Model I with element size  $h^e = 0.002$  mm.  $u_1 = 0$  mm,  $u_2 = 0.2$  mm,  $u_3 = 0.378$  mm,  $u_4 = 0.458$  mm,  $u_5 = 0.478$  mm,  $u_6 = 0.498$  mm,  $u_7 = 0.518$  mm,  $u_8 = 0.538$  mm,  $u_9 = 0.545$  mm

For Rubber Fracture Model II, Figure 6.11 shows the deformed geometry at points (a) through (k) on the load-displacement curve in Figure 6.9. To aid visualization of the damage, elements with  $d > 0.95$  are removed from the plot. Figure 6.11a is the initial configuration of the specimen. Figure 6.11b is the first point where the damage has initiated. At Point c, damage is still increasing, but crack has not been propagated yet. After the Point d, a small crack zone becomes observable and material starts to lose its stress bearing capacity. Further stretching results in sudden crack propagation. Note that, the displacement and time increments between Points e,f, and g are same in Figure 6.9. In Points g, h, and i in Figure 6.11 material has already lost its bearing capacity. Point j shows the fully fractured material.

For Rubber Fracture Model II, Figure 6.10 shows the load-displacement curve for the

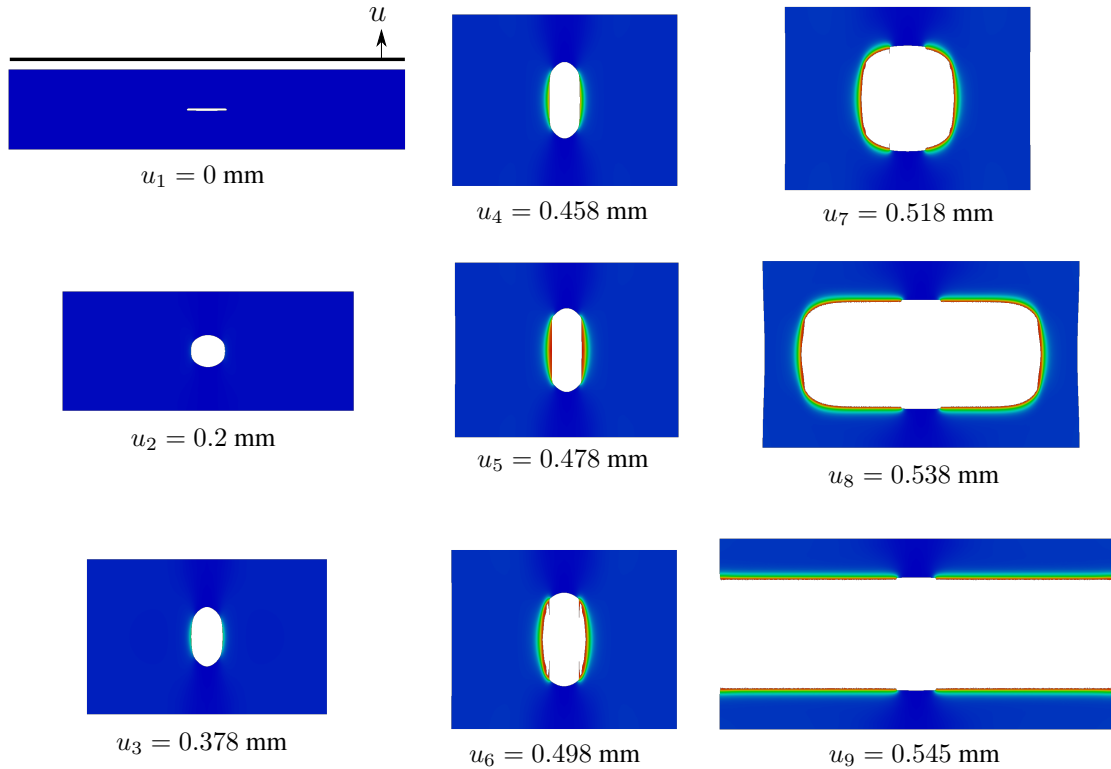


Figure 6.4: Corresponding deformed shapes of the specimen for the tension test given in Figure 6.3

double-notch specimen with different initial notch lengths. In this numerical analysis, non-affinity parameter has taken different than  $p = 2$ . Further analysis should be conducted for determine the material parameter set in order to reflect the experimental results more accurately.

## 6.1 Discussion of Numerical Results

Although the load carrying capacity of double-notched specimen decreases with increasing notch length, they do not coincide with the experimental data. In Rubber Fracture Model I, although the same material parameters as in the [20] study have been used, they could not be fitted to the experimental data, Figure 6.7b. The main reason for this problem may be that the simulation was performed with plane strain conditions, although the experimental study was more suitable for plane stress as-

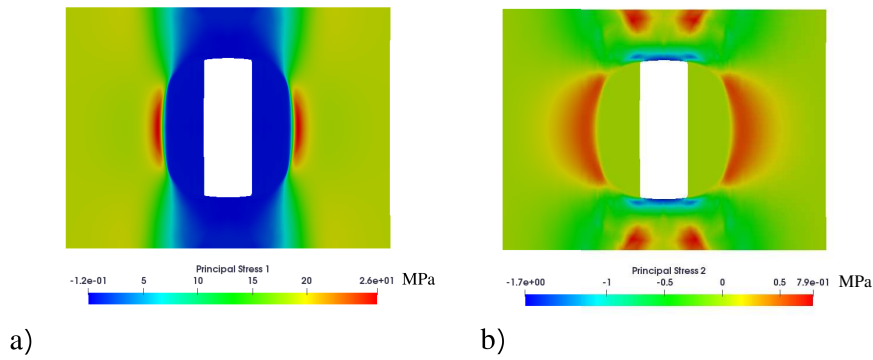


Figure 6.5: Principal stresses for Fracture Model I with penny shaped precracked test specimen,  $u = 0.518$  mm.

sumption. However, more realistic results for the presented model can be obtained by performing a parameter analysis for the plane stress condition. In Rubber Fracture Model II, although the material parameters in the study [25] have been used, the fracture displacement in the simulations underestimate the experimental data, Figure 6.8. The inaccuracy of the material parameters may cause this problem. However, the consistency of the results in itself indicates that the model will offer promising results with appropriate material parameters as shown in Figure 6.10.

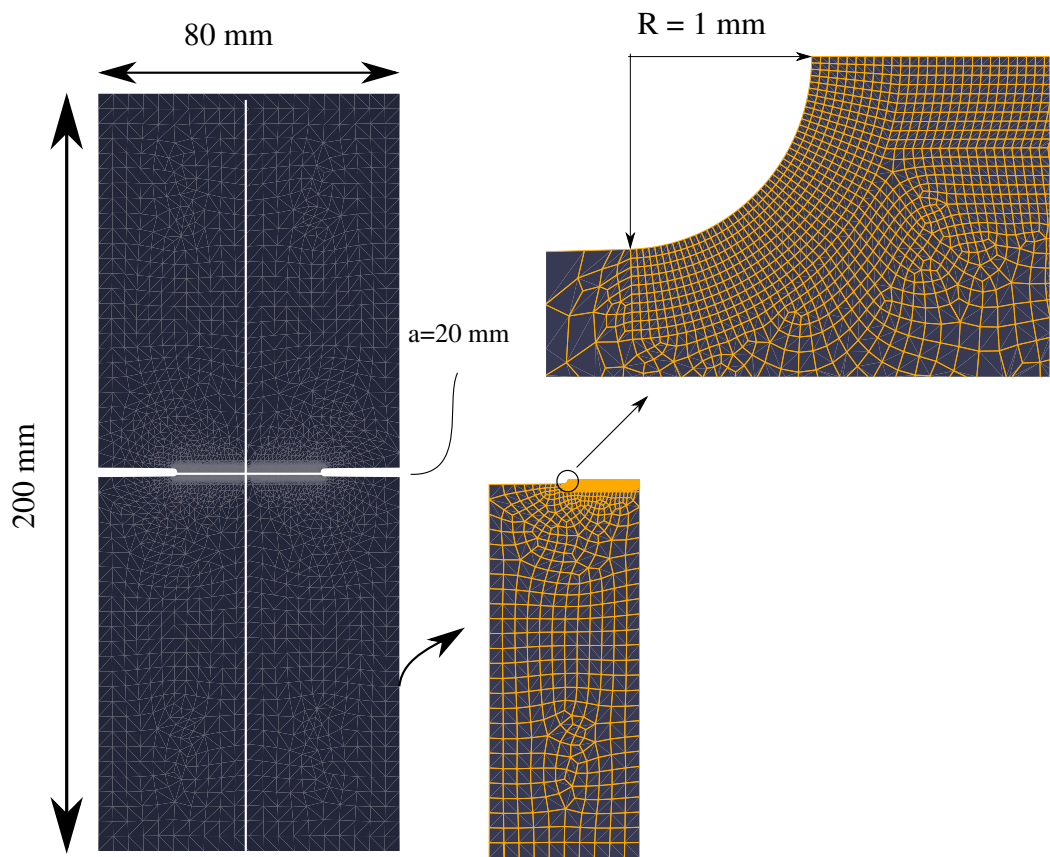


Figure 6.6: Mesh for double-notch specimen and crack region.

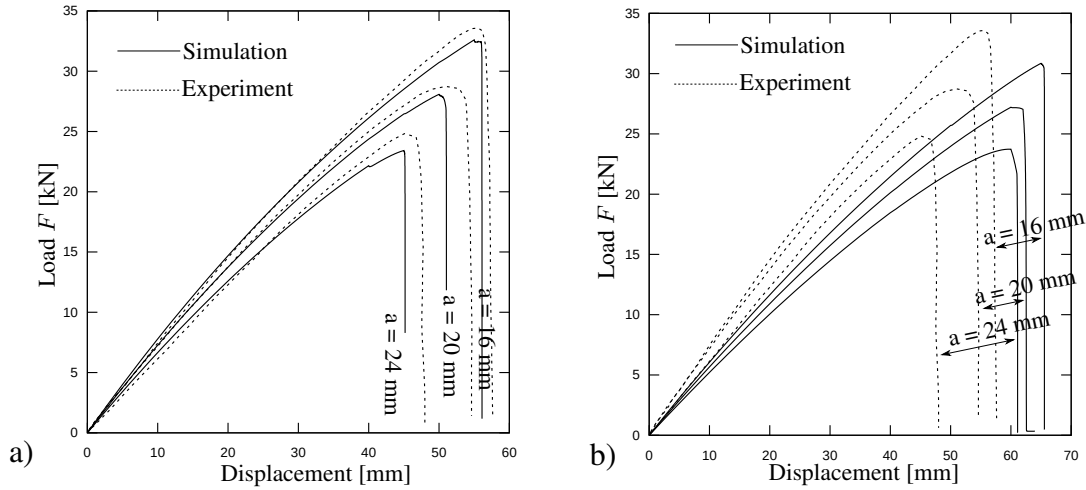


Figure 6.7: a) Comparison of the numerical results of Rubber Fracture Model I with experimental data in plane-strain solution. b) Comparison of the numerical results of Rubber Fracture Model I with experimental data in plane-stress solution. The chosen material parameters  $\mu = 0.203$  N/mm<sup>2</sup>,  $\nu = 0.45$ ,  $g_c = 2.67$  N/mm,  $l = 1.0$  mm,  $\eta = 1.0 \times 10^{-3}$  mm.

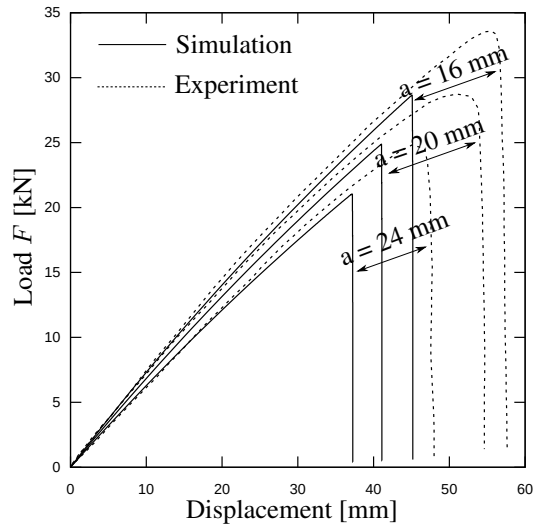


Figure 6.8: Comparison of load-deflection curves for Rubber Fracture Model II from simulations against the experimental results of [1] with chosen material parameters  $K = 2.68$  N/mm<sup>2</sup>,  $\mu = 0.268$  N/mm<sup>2</sup>,  $N = 1000$ ,  $p = 2.0$ ,  $\bar{E}_b = 2.67$  N/mm<sup>2</sup>,  $\varepsilon^f = 0.235$  N/mm,  $l = 1.0$  mm,  $\eta = 1.0 \times 10^{-2}$  MPa · s

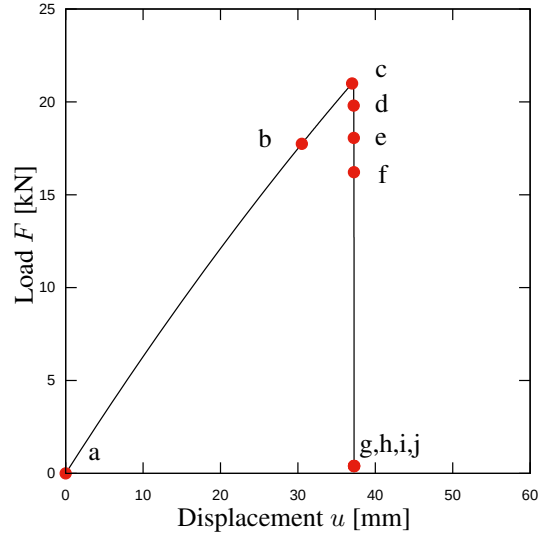


Figure 6.9: Load-displacement curve of double-edge-notched tension specimen for Rubber Fracture Model II with initial crack length  $a = 16$  mm.  $u_a = 0.0$  mm,  $u_b = 30.5$  mm,  $u_c = 37.0$  mm,  $u_d = 37.214$  mm,  $u_e = 37.229$  mm,  $u_f = 37.239$  mm,  $u_g = 37.249$  mm,  $u_h = 37.259$  mm,  $u_i = 37.261$  mm,  $u_j = 37.262$  mm.

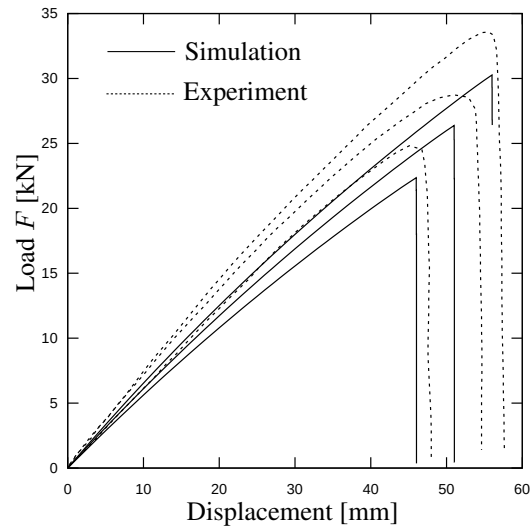


Figure 6.10: Comparison of load-deflection curves for Rubber Fracture Model II from simulations against the experimental results of [1] with chosen material parameters  $\mu = 0.268$  N/mm<sup>2</sup>,  $N = 1000$ ,  $\bar{E}_b = 2.67$  N/mm<sup>2</sup>,  $K = 2.68$  N/mm<sup>2</sup>,  $\varepsilon^f = 0.240$  N/mm,  $l = 1.0$  mm,  $\eta = 1.0 \times 10^{-2}$  MPa  $\cdot$  s,  $p = 1.47$ .

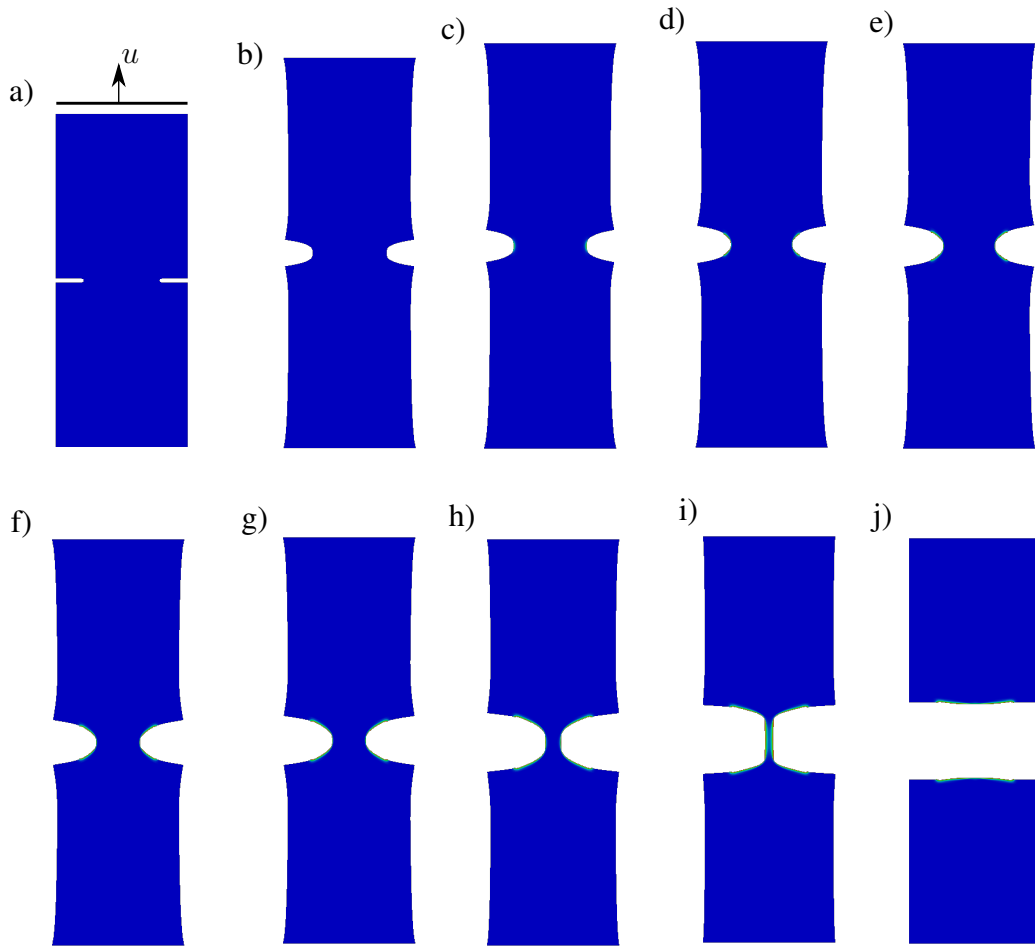


Figure 6.11: Deformed geometry of double-edge-notched tension specimen for different displacement values given in Figure 6.9.

## CHAPTER 7

### CONCLUDING REMARKS

The failure analysis of rubbery polymers which show high nonlinear material behavior at large deformations was numerically modeled in this thesis. The rupture of rubbery polymers has been modeled by using the Phase-Field method where the conservation equation of linear momentum and the evolution equation crack phase-field are solved together. The material behavior of rubbery polymers undergoing damage has been modeled by two distinct approaches taken from literature where the damage-induced degradation in the material affects either the entropic and volumetric part of the energy or the energetic and volumetric part of the energy. Furthermore, for the entropic elasticity distinct constitutive approaches has been implemented to observe the high non-linear material behavior. Several modeling approaches has been studied to make a comparison through numerical analysis of benchmark problems with highly heterogeneous deformations of rubbery polymers undergoing rupture.

In Rubber Fracture Model II, the free energy contribution of the single-chain is not multiplied with the degradation function  $g(d)$ . To this end,  $\lambda_b$  parameter increases the chain resting length and increases the number of possible configurations. Therefore, single-chain contribution decreases and the infinite response of the single-chain remains finite for the larger values of stretch. With an increasing number of possible configurations, entropy begins to increase. Once the critical crack driving force  $\varepsilon^f$  is reached, damage starts to initiate and decreases the energetic and volumetric contribution. The power of the bond stretch model comes from the energetic and entropic split, both controlled by one internal variable  $\lambda_b$ , which increases the crack driving force  $\mathcal{H}$ . In the light of this discussion, we did not use the tube contribution proposed in the microsphere model, because the contribution of the tube will not reach to a

finite value. Another area contraction variable could be added to the proposed model with an appropriate minimization principle similar to Equation (5.81).

Based on our investigations, the stability of the solution of the coupled failure problem is highly dependent on the mesh size and mesh structure due to the extreme deformations of the elements in the crack path. In order to overcome the mesh distortion problem, the arbitrary Lagrangian-Eulerian finite element formulation could be considered as future work. Moreover, crack tips in the tearing zone have high velocity due to the sudden crack propagation, especially in the late stages of failure. For that reason, a dynamic solution scheme may be more suitable than the quasi-static solution scheme for the failure analysis of the rubbery polymers. Furthermore, as a future work, the viscoelastic effects of the rubber should be considered in order to express the time-dependent behavior of the rubber and estimate the fatigue resistance under cyclic loading. Moreover, for non-monotonous loadings, the damage-induced degradation function should be extended to account for tension-compression asymmetry to avoid interpenetration of the crack lips. Also, the effect of strain-induced crystallization should be studied in order to express the stiffening response and increased crack resistance of rubber.

## REFERENCES

- [1] N. Aït Hocine, M. Abdelaziz, and A. Imad, “Fracture problems of rubbers : J-integral estimation based upon  $\eta$  factors and investigation on the strain energy density distribution as a local criterion,” *International Journal of Fracture*, vol. 117, pp. 1–23, 2002.
- [2] A. A. Griffith and G. I. Taylor, “VI. The phenomena of rupture and flow in solids,” *Philosophical Transactions of the Royal Society of London. Series A, Containing Papers of a Mathematical or Physical Character*, vol. 221, pp. 163–198, 1921.
- [3] G. R. Irwin, *Fracture*. Berlin, Heidelberg: Springer, 1958.
- [4] G. Barenblatt, “The mathematical theory of equilibrium cracks in brittle fracture,” vol. 7 of *Advances in Applied Mechanics*, pp. 55 – 129, Elsevier, 1962.
- [5] B. Bourdin, G. A. Francfort, and J.-J. Marigo, “The variational approach to fracture,” *Journal of Elasticity*, vol. 91, pp. 5–148, 2008.
- [6] G. Francfort and J.-J. Marigo, “Revisiting brittle fracture as an energy minimization problem,” *Journal of the Mechanics and Physics of Solids*, vol. 46, pp. 1319 – 1342, 1998.
- [7] C. Chen, Z. Wang, and Z. Suo, “Flaw sensitivity of highly stretchable materials,” *Extreme Mechanics Letters*, vol. 10, pp. 50 – 57, 2017.
- [8] R. S. Rivlin and A. G. Thomas, “Rupture of rubber. I. Characteristic energy for tearing,” *Journal of Polymer Science*, vol. 10, pp. 291–318, 1953.
- [9] G. J. Lake, A. G. Thomas, and D. Tabor, “The strength of highly elastic materials,” *Proceedings of the Royal Society of London. Series A. Mathematical and Physical Sciences*, vol. 300, pp. 108–119, 1967.

- [10] B. N. J. Persson, O. Albohr, G. Heinrich, and H. Ueba, “Crack propagation in rubber-like materials,” *Journal of Physics: Condensed Matter*, vol. 17, no. 44, pp. 1071–1142, 2005.
- [11] M. Kroon, “Steady-state crack growth in rubber-like solids,” *International Journal of Fracture*, vol. 169, pp. 49–60, 2011.
- [12] B. N. J. Persson and E. A. Brener, “Crack propagation in viscoelastic solids,” *Phys. Rev. E*, vol. 71, p. 036123, 2005.
- [13] J. Fineberg and M. Marder, “Instability in dynamic fracture,” *Physics Reports*, vol. 313, pp. 1 – 108, 1999.
- [14] S. Göktepe and C. Miehe, “A micro–macro approach to rubber-like materials. Part III: The micro-sphere model of anisotropic mullins-type damage,” *Journal of the Mechanics and Physics of Solids*, vol. 53, pp. 2259–2283, 2005.
- [15] E. Ducrot, Y. Chen, M. Bulters, R. Sijbesma, and C. Creton, “Toughening elastomers with sacrificial bonds and watching them break,” *Science (New York, N.Y.)*, vol. 344, pp. 186–189, 2014.
- [16] H. Brown, “A model of the fracture of double network gels,” *Macromolecules*, vol. 40, pp. 3815–3818, 2007.
- [17] Y. Mao and L. Anand, “A theory for fracture of polymeric gels,” *Journal of the Mechanics and Physics of Solids*, vol. 115, pp. 30 – 53, 2018.
- [18] L. Böger, M.-A. Keip, and C. Miehe, “Minimization and saddle-point principles for the phase-field modeling of fracture in hydrogels,” *Computational Materials Science*, vol. 138, pp. 474 – 485, 2017.
- [19] B. Bourdin, G. Francfort, and J.-J. Marigo, “Numerical experiments in revisited brittle fracture,” *Journal of the Mechanics and Physics of Solids*, vol. 48, pp. 797–826, 2000.
- [20] C. Miehe and L.-M. Schänzel, “Phase field modeling of fracture in rubbery polymers. Part I: Finite elasticity coupled with brittle failure,” *Journal of the Mechanics and Physics of Solids*, vol. 65, pp. 93 – 113, 2014.

- [21] C. Miehe, L.-M. Schänzel, and H. Ulmer, “Phase field modeling of fracture in multi-physics problems. Part I: Balance of crack surface and failure criteria for brittle crack propagation in thermo-elastic solids,” *Computer Methods in Applied Mechanics and Engineering*, vol. 294, pp. 449 – 485, 2015.
- [22] A. Kumar, G. A. Francfort, and O. Lopez-Pamies, “Fracture and healing of elastomers: A phase-transition theory and numerical implementation,” *Journal of the Mechanics and Physics of Solids*, vol. 112, pp. 523 – 551, 2018.
- [23] C. Miehe, F. Welschinger, and M. Hofacker, “Thermodynamically consistent phase-field models of fracture: Variational principles and multi-field FE implementations,” *International Journal for Numerical Methods in Engineering*, vol. 83, pp. 1273–1311, 2010.
- [24] A. Raina and C. Miehe, “A phase-field model for fracture in biological tissues,” *Biomechanics and Modeling in Mechanobiology*, vol. 15, pp. 479–496, 2016.
- [25] B. Talamini, Y. Mao, and L. Anand, “Progressive damage and rupture in polymers,” *Journal of the Mechanics and Physics of Solids*, vol. 111, pp. 434 – 457, 2018.
- [26] S. Teichtmeister, D. Kienle, F. Aldakheel, and M.-A. Keip, “Phase field modeling of fracture in anisotropic brittle solids,” *International Journal of Non-Linear Mechanics*, vol. 97, pp. 1 – 21, 2017.
- [27] M. Hofacker and C. Miehe, “Continuum phase field modeling of dynamic fracture: Variational principles and staggered FE implementation,” *International Journal of Fracture*, vol. 178, pp. 113–129, 2012.
- [28] M. J. Borden, T. J. Hughes, C. M. Landis, and C. V. Verhoosel, “A higher-order phase-field model for brittle fracture: Formulation and analysis within the isogeometric analysis framework,” *Computer Methods in Applied Mechanics and Engineering*, vol. 273, pp. 100 – 118, 2014.
- [29] M. Hofacker and C. Miehe, “A phase field model of dynamic fracture: Robust field updates for the analysis of complex crack patterns,” *International Journal for Numerical Methods in Engineering*, vol. 93, pp. 276–301, 2013.

- [30] M. Ambati, T. Gerasimov, and L. De Lorenzis, “Phase-field modeling of ductile fracture,” *Computational Mechanics*, vol. 55, pp. 1017–1040, 2015.
- [31] C. Miehe, M. Hofacker, L.-M. Schänzel, and F. Aldakheel, “Phase field modeling of fracture in multi-physics problems. Part II: Coupled brittle-to-ductile failure criteria and crack propagation in thermo-elastic–plastic solids,” *Computer Methods in Applied Mechanics and Engineering*, vol. 294, pp. 486 – 522, 2015.
- [32] J.-Y. Wu, V. P. Nguyen, C. T. Nguyen, D. Sutula, S. Sinaie, and S. Bordas, “Phase-field modeling of fracture,” vol. 53 of *Advances in Applied Mechanics*, Elsevier, 2019.
- [33] L. Treloar, *The Physics of Rubber Elasticity*. Oxford Classic Texts in the Physical Sciences, Oxford University Press, USA, 1975.
- [34] E. M. Arruda and M. C. Boyce, “A three-dimensional constitutive model for the large stretch behavior of rubber elastic materials,” *Journal of the Mechanics and Physics of Solids*, vol. 41, pp. 389 – 412, 1993.
- [35] C. Miehe, S. Göktepe, and F. Lulei, “A micro-macro approach to rubber-like materials—Part I: The non-affine micro-sphere model of rubber elasticity,” *Journal of the Mechanics and Physics of Solids*, vol. 52, pp. 2617 – 2660, 2004.
- [36] B. D. Coleman and W. Noll, “The thermodynamics of elastic materials with heat conduction and viscosity,” in *The Foundations of Mechanics and Thermodynamics*, pp. 145–156, Springer, 1974.
- [37] G. Holzapfel, *NONLINEAR SOLID MECHANICS. A Continuum Approach for Engineering*. John Wiley & Sons, Newyork, 2001.
- [38] E. Tadmor, R. Miller, and R. Elliott, *Continuum mechanics and thermodynamics: From fundamental concepts to governing equations*. Cambridge University Press, 2011.
- [39] S. Göktepe, *Micro-macro approaches to rubbery and glassy polymers: Predictive micromechanically-based models and simulations*. PhD thesis, University of Stuttgart, 2007.

- [40] V. Lubarda, “On thermodynamic potentials in linear thermoelasticity,” *International Journal of Solids and Structures*, vol. 41, pp. 7377–7398, 2004.
- [41] C. Miehe, “Aspects of the formulation and finite element implementation of large strain isotropic elasticity,” *International Journal for Numerical Methods in Engineering*, vol. 37, pp. 1981–2004, 1994.
- [42] J. Bonet and R. D. Wood, *Nonlinear Continuum Mechanics for Finite Element Analysis*. Cambridge University Press, 2 ed., 2008.
- [43] G. Marckmann and E. Verron, “Comparison of hyperelastic models for rubber-like materials,” *Rubber Chemistry and Technology*, vol. 79, pp. 835–858, 2006.
- [44] M. C. Boyce and E. M. Arruda, “Constitutive models of rubber elasticity: A review,” *Rubber Chemistry and Technology*, vol. 73, pp. 504–523, 2000.
- [45] G. Saccomandi and R. W. Ogden, eds., *Mechanics and Thermomechanics of Rubberlike Solids*. Springer, Vienna, 2004.
- [46] J. E. Mark and B. Erman, *Rubberlike Elasticity: A Molecular Primer*. Cambridge University Press, 2 ed., 2007.
- [47] H. M. James and E. Guth, “Theory of the elastic properties of rubber,” *The Journal of Chemical Physics*, vol. 11, pp. 455–481, 1943.
- [48] P. Flory, *Statistical mechanics of chain molecules*. Interscience Publishers, 1969.
- [49] M. Doi and S. Edwards, *The Theory of Polymer Dynamics*. Comparative Pathobiology - Studies in the Postmodern Theory of Education, Clarendon Press, 1988.
- [50] M. C. Wang and E. Guth, “Statistical theory of networks of non-gaussian flexible chains,” *The Journal of Chemical Physics*, vol. 20, pp. 1144–1157, 1952.
- [51] P. Bažant and B. H. Oh, “Efficient numerical integration on the surface of a sphere,” *ZAMM - Journal of Applied Mathematics and Mechanics / Zeitschrift für Angewandte Mathematik und Mechanik*, vol. 66, pp. 37–49, 1986.

- [52] E. Verron, “Questioning numerical integration methods for microsphere (and microplane) constitutive equations,” *Mechanics of Materials*, vol. 89, pp. 216 – 228, 2015.
- [53] C. Kuhn, A. Schlüter, and R. Müller, “On degradation functions in phase field fracture models,” *Computational Materials Science*, vol. 108, pp. 374 – 384, 2015.
- [54] R. L. Taylor, “FEAP - Finite Element Analysis Program,” 2014.
- [55] S. Klinkel and S. Govindjee, “Using finite strain 3D-material models in beam and shell elements,” *Engineering Computations*, vol. 19, pp. 902–921, 2002.
- [56] O. Zienkiewicz, R. Taylor, and D. Fox, *The Finite Element Method for Solid and Structural Mechanics*. Oxford: Butterworth-Heinemann, seventh ed., 2014.
- [57] D. Systèmes, “Abaqus 6.10: Analysis user’s manual,” *Providence, RI: Dassault Systèmes Simulia Corp*, 2010.